Remnants of early Earth differentiation in the deepest mantle-derived lavas

Andrea Giuliani[a,b,1], Matthew G. Jackson[c], Angus Fitzpayne[a], and Hayden Dalton[b]

[a]Institute of Geochemistry and Petrology, Department of Earth Sciences, ETH Zurich, 8092 Zurich, Switzerland; [b]Kimberlites and Diamonds, School of Earth Sciences, The University of Melbourne, Parkville, VIC 3010, Australia; and [c]Department of Earth Science, University of California, Santa Barbara, CA 93106

Edited by Donald J. DePaolo, Lawrence Berkeley National Laboratory, Berkeley, CA, and approved November 18, 2020 (received for review July 18, 2020)

The noble gas isotope systematics of ocean island basalts suggest the existence of primordial mantle signatures in the deep mantle. Yet, the isotopic compositions of lithophile elements (Sr, Nd, Hf) in these lavas require derivation from a mantle source that is geochemically depleted by melt extraction rather than primitive. Here, this apparent contradiction is resolved by employing a compilation of the Sr, Nd, and Hf isotope composition of kimberlites—volcanic rocks that originate at great depth beneath continents. This compilation includes kimberlites as old as 2.06 billion years and shows that kimberlites do not derive from a primitive mantle source but sample the same geochemically depleted component (where geochemical depletion refers to ancient melt extraction) common to most oceanic island basalts, previously called PREMA (prevalent mantle) or FOZO (focal zone). Extrapolation of the Nd and Hf isotopic compositions of the kimberlite source to the age of Earth formation yields a $^{143}Nd/^{144}Nd$-$^{176}Hf/^{177}Hf$ composition within error of chondrite meteorites, which include the likely parent bodies of Earth. This supports a hypothesis where the source of kimberlites and ocean island basalts contains a long-lived component that formed by melt extraction from a domain with chondritic $^{143}Nd/^{144}Nd$ and $^{176}Hf/^{177}Hf$ shortly after Earth accretion. The geographic distribution of kimberlites containing the PREMA component suggests that these remnants of early Earth differentiation are located in large seismically anomalous regions corresponding to thermochemical piles above the core–mantle boundary. PREMA could have been stored in these structures for most of Earth's history, partially shielded from convective homogenization.

mantle evolution | early Earth | kimberlite | ocean island basalt | LLSVP

Oceanic basalts provide a more direct approach to investigate Earth's convecting mantle than mantle-derived continental magmas, as they erupt on oceanic lithosphere, which is considerably thinner and less enriched in mantle-incompatible elements than the lithosphere of continental plates. Hence, most of what is currently known about Earth's convecting mantle—the most voluminous domain of our planet—derives from the study of oceanic basalts. One obvious drawback is that this knowledge is largely limited to the last 150 to 200 My (i.e., the oldest age of oceanic lithosphere before it is subducted).

Ocean island basalts (OIBs) derive from partial melting of mantle plumes, the majority of which are associated with seismically anomalous regions called large low shear-wave velocity provinces (LLSVPs) located above the core–mantle boundary (1, 2). OIBs exhibit He isotope compositions that can extend to considerably less radiogenic values (i.e., higher $^3He/^4He$ ratios) compared with mid-ocean ridge basalts (MORBs), which has been widely advocated as evidence that the source of OIBs contains a primordial component preserved since Earth accretion (3). The Xe isotope systematics of some high-$^3He/^4He$ OIBs further indicate that their source region became separated from the MORB source within the first 100 My of Earth accretion (4), where the MORB source occupies most of Earth's convecting mantle and is geochemically depleted in incompatible elements due to continuous extraction of oceanic and continental crust from the mantle (5, 6). Elevated $^3He/^4He$ ratios in OIBs appear to be exclusively associated with plumes originating from the LLSVPs (7, 8), thus suggesting a possible spatial link between early Earth remnants and these seismically anomalous regions above the core–mantle boundary.

Elevated $^3He/^4He$ ratios may be a common feature of the prevalent mantle (PREMA) (9, 10). This mantle component was originally defined using the narrow range of Nd and Sr isotope ratios (e.g., $^{143}Nd/^{144}Nd \sim 0.5129$ to 0.5130) shown by several OIBs (10). In Sr-Nd-Pb isotope plots, OIBs from each island chain form compositional trends that converge from variously enriched compositions to a common moderately depleted mantle component dubbed focal zone [FOZO (9)], which has a radiogenic isotope composition like that of PREMA (10, 11) (Fig. 1). This implies that FOZO and PREMA are essentially equivalent, and we treat them as such in this manuscript. These observations have been widely employed to argue that PREMA represents a fundamental and abundant constituent of Earth's convecting mantle, which contributes to the genesis of most OIBs [and also some MORBs (12, 13)]. This interpretation is reinforced by the common occurrence of PREMA-like compositions in juvenile continental magmas (10, 11, 14, 15) and as we will show, in kimberlites dating back to more than ∼2 Ga.

The association between primordial high-$^3He/^4He$ compositions with nonchondritic high-$^{143}Nd/^{144}Nd$ ratios—indicative of long-term depletion in PREMA—apparently negates a primitive origin of PREMA (16). However, these apparently contradictory geochemical features could be reconciled if PREMA represents a depleted mantle residue that formed by silicate melt extraction in the early Earth (10). Alternatively, PREMA could originate

Significance

Understanding how the Earth evolved from its accretion to the present-day conditions is a major quest of the Earth sciences. This contribution focuses on the evolution of the deepest realms of our planet sampled by basalts in ocean islands (such as Hawaii) during the last ∼100 to 150 million years and diamond-bearing kimberlites emplaced in continents since ∼2 billion years ago. Radiogenic isotope ratios are employed to demonstrate that these lavas share a common source, which includes a component that originated from melt extraction soon after Earth accretion. These findings help reconcile contrasting geochemical observations in ocean island basalts and provide constraints on the composition and evolution of the deepest and most ancient parts of Earth's mantle.

Author contributions: A.G. designed research; A.G. and M.G.J. performed research; A.G., A.F., and H.D. analyzed data; and A.G. and M.G.J. wrote the paper with contributions from A.F. and H.D.

The authors declare no competing interest.

This article is a PNAS Direct Submission.

[1]To whom correspondence may be addressed. Email: andrea.giuliani@erdw.ethz.ch.

This article contains supporting information online at https://www.pnas.org/lookup/suppl/doi:10.1073/pnas.2015211118/-/DCSupplemental.

Published December 28, 2020.

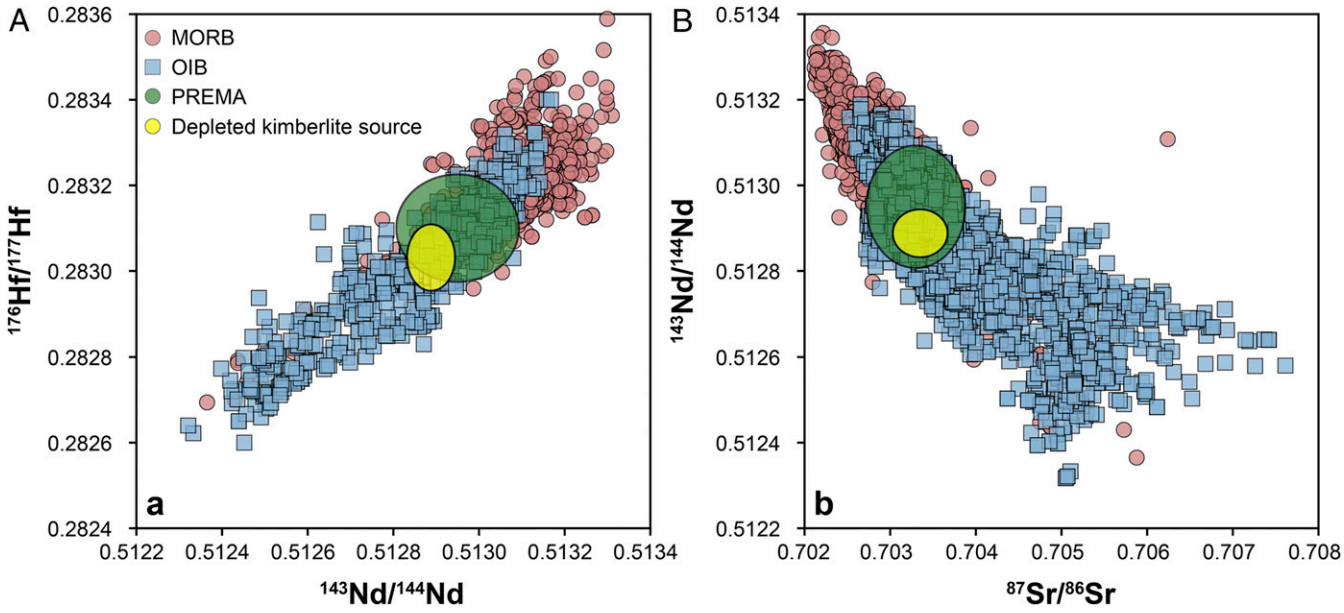

Fig. 1. Present-day Sr-Nd-Hf isotope compositions of MORB and OIBs including the overlapping positions of the OIB-based PREMA or FOZO and depleted kimberlite source. (*A*) $^{143}Nd/^{144}Nd$ vs. $^{176}Hf/^{177}Hf$; (*B*) $^{87}Sr/^{86}Sr$ vs. $^{143}Nd/^{144}Nd$. The OIB–PREMA corresponds to the Geochemical Centre of Konter et al. (33) (*Materials and Methods* show the calculation of $^{176}Hf/^{177}Hf$), while the depleted kimberlite source is from this study (Fig. 2); the PREMA ellipses represent calculated values ±2σ uncertainties. MORB and OIB values are from the compilation of Stracke (11).

from mixing of geochemically depleted and enriched components, specifically mixing the MORB source (or depleted mid-ocean ridge basalt mantle [DMM]) with enriched recycled lithologies that are introduced into the convecting mantle via subduction (10, 13, 14). This hypothesis would not predict that PREMA has primordial noble gas signatures including high $^{3}He/^{4}He$ because DMM and recycled lithologies have low $^{3}He/^{4}He$.

Insights into this long-standing and yet not fully resolved association between primordial noble gas isotope signatures and geochemically depleted lithophile element (Sr, Nd, Hf) isotope compositions in OIBs could be provided by kimberlites, the deepest-derived magmatic rocks that occur in continents. Kimberlites contain He and Ne isotope signatures similar to those of OIBs (17), including elevated $^{3}He/^{4}He$ ratios (18), and a recent compilation of the Nd-Hf isotope compositions of kimberlites through time argued that they sample a primitive mantle source with circa-chondritic composition over much of geologic time (19). In this context, chondrite meteorites represent the likely building blocks of Earth. In addition, the majority of Phanerozoic kimberlites show a geographic correspondence to the margins of the African LLSVP in the lower mantle at the time of their eruption (20), and some kimberlite fields occur along age-progressive corridors corresponding to the continental portions of OIB (hot-spot) tracks in ocean basins (21). These lines of evidence suggest that kimberlites might sample deep mantle sources similar to OIBs. However, kimberlites have been emplaced in continental regions since at least ∼2.1 Ga and perhaps, since 2.8 Ga (22) and hence, provide a record of deep and ancient mantle components that spans a time window more than an order of magnitude longer than that represented by OIBs (i.e., <200 Ma).

To understand if primitive mantle is preserved in the deep Earth and sampled by kimberlites (19) and constrain its relationship to the LLSVPs, here we interrogate an Sr-Nd-Hf isotope compilation of kimberlites and closely related magmatic rocks named ultramafic lamprophyres, which were emplaced in the upper crust since 2.06 Ga. These carbonate-rich, silica-poor magmas are generated by low-degree partial melting of the sublithospheric (i.e., convecting) mantle beneath thick continental regions (cratons and surrounding belts) (23–25). Crustal assimilation in these magmas is limited by their rapid ascent, lack of processing in magma chambers, and high mantle-incompatible trace element concentrations. Therefore, the radiogenic isotope compositions ($^{87}Sr/^{86}Sr$, $^{143}Nd/^{144}Nd$, $^{176}Hf/^{177}Hf$) of kimberlites provide a more robust record of deep mantle evolution (i.e., less prone to crustal contamination) than common silicate magmas such as continental basalts (19, 24, 26). In the following, we take advantage of the long half-lives of the ^{87}Rb-^{87}Sr (half-life = 49 Gy), ^{147}Sm-^{143}Nd (106 Gy), and ^{176}Lu-^{176}Hf (37 Gy) systems, which allow for closed system evolution of these decay systems to be considered linear over the lifetime of the solar system.

The Radiogenic Isotope Record of Kimberlites through Time

In order to evaluate the time evolution of kimberlites, it is important to first define a suite of kimberlitic compositions that best reflect their respective mantle sources. The term "kimberlite" has been previously (and incorrectly) employed to describe different types of diamond-bearing magmas, including rocks (e.g., group II kimberlites, also called orangeites) with an affinity to magmas derived from metasomatized (i.e., geochemically enriched by mantle fluids) lithospheric mantle sources (24). In this paper, a robust screening based on a strict definition of kimberlites is applied (27) (*Materials and Methods*). This compilation includes Nd and Hf isotope compositions of bulk kimberlite samples, including some Nd isotope ratios for perovskite separates, from worldwide localities (*SI Appendix*, Fig. S1) with well-constrained emplacement ages (Dataset S1). The Sr isotope data are less comprehensive because they are restricted to analyses of perovskite, a robust magmatic phase, given that crustal contamination commonly modifies the magmatic Sr isotope signature of kimberlite rocks (24). We attempted to address the influence of crustal contamination on bulk rock Nd and Hf isotope compositions by applying major and trace element-based filters (e.g., Si/Al, Nb/Th, Ba/Nb, Ce/Pb) that are extremely sensitive to continental crust contributions (28, 29). With rare exceptions (30), major and trace element ratios are not correlated to the Nd-Hf isotopic compositions in kimberlites (*SI Appendix*, Figs. S2–S6). This observation is consistent with the occurrence of magmatic, mantle, and crustal components in bulk kimberlites (27). However, kimberlite

magmas are highly enriched in Nd and to a lesser extent, Hf compared with common mantle and crustal rocks (24, 28, 29). Any contribution from crustal or enriched (i.e., metasomatized) lithospheric mantle components would lower the $^{143}Nd/^{144}Nd$ and $^{176}Hf/^{177}Hf$ and increase the $^{87}Sr/^{86}Sr$ ratios of kimberlite magmas (26, 30). Also, hydrothermal alteration, which is common in kimberlites (27), is unlikely to modify bulk rock Sm/Nd and Lu/Hf ratios due to the fluid-immobile behavior of these elements. Therefore, rather than filtering the bulk kimberlite Nd-Hf isotope data for crustal or lithospheric mantle contamination using major and trace element ratios, only the most radiogenic bulk rock $^{143}Nd/^{144}Nd$ and $^{176}Hf/^{177}Hf$ value and the least radiogenic perovskite $^{87}Sr/^{86}Sr$ value in each kimberlite province are considered, as these are least likely to have been influenced by lithospheric contamination, including continental crust assimilation (*Materials and Methods*). These isotopic values are hereafter considered representative of the evolution of the deep, sublithospheric mantle source of kimberlites through time.

When the initial Sr, Nd, and Hf isotope compositions of all kimberlites are plotted as a function of time (Fig. 2), kimberlites from each province have compositions that range from moderately depleted (i.e., higher $^{143}Nd/^{144}Nd$, $^{176}Hf/^{177}Hf$, and lower $^{87}Sr/^{86}Sr$ corresponding to long-term evolution under high Sm/Nd and Lu/Hf and low Rb/Sr) to more geochemically enriched isotopic values (i.e., lower $^{143}Nd/^{144}Nd$, $^{176}Hf/^{177}Hf$, and higher $^{87}Sr/^{86}Sr$). A first-order observation is that kimberlites do not exhibit extreme depletion and thus, never extend to DMM (i.e., MORB source) compositions. Some <200-Ma kimberlites (i.e., North America Central Corridor and Lac de Gras in Canada, Alto Paranaiba in Brazil, and South Australia) are unusual in that they are geochemically enriched and exhibit isotopic compositions that overlap with the EM-1 (enriched mantle type-1; which contains deeply subducted crustal material) compositions in OIBs (*SI Appendix*, Fig. S7). In detail, Sr isotope compositions in these kimberlites are limited to higher $^{87}Sr/^{86}Sr$ (i.e., more geochemically enriched compositions) compared with other kimberlites and ultramafic lamprophyres of similar age (e.g., Tanzania, Rosario do Sul [Brazil], Siberia Jurassic) (Fig. 2). This observation is in line with the interpretation of Woodhead et al. (19), where the sources of kimberlites emplaced in the past 200 Ma near the margins of Pangea are influenced by addition of deeply subducted, recycled crustal material. Whether or not this phenomenon had a limited impact on kimberlites earlier in geologic time is unclear based on our database, which shows variability in initial $^{143}Nd/^{144}Nd$ and especially $^{87}Sr/^{86}Sr$ and $^{176}Hf/^{177}Hf$ ratios at any given time in the kimberlite record. After these anomalous, geochemically enriched kimberlites are excluded, a remarkable pattern becomes clear, wherein the most unradiogenic Sr and most radiogenic Nd-Hf isotope compositions in each kimberlite province plot along a relatively narrow linear array through time (Fig. 2). This observation appears to indicate that a common, moderately depleted component (less depleted than the upper mantle source of MORB) has participated in the genesis of kimberlites since at least 2.06 Ga. The spread of isotopic values toward more geochemically enriched compositions (i.e., lower $^{143}Nd/^{144}Nd$, $^{176}Hf/^{177}Hf$, and higher $^{87}Sr/^{86}Sr$) recorded by kimberlites in each province at a given time can be related to different factors including crustal contamination (30), contribution by enriched lithospheric mantle (25, 31), or source pollution by recycled crustal material (19, 26, 32).

Kimberlites and the Origin of PREMA

Statistically robust regressions (*Materials and Methods*) through the common depleted component of kimberlites in plots of Sr-Nd-Hf isotope ratios vs. time (Fig. 2) yield present-day compositions ($^{143}Nd/^{144}Nd = 0.512897 \pm 0.000060$ [2σ; i.e., $\varepsilon^{143}Nd = 5.2 \pm 1.2$]; $^{176}Hf/^{177}Hf = 0.283013 \pm 0.000076$ [i.e., $\varepsilon^{176}Hf = 8.1 \pm 2.7$]; $^{87}Sr/^{86}Sr = 0.70335 \pm 0.00032$) within the PREMA (or FOZO) field sampled by OIBs ($^{143}Nd/^{144}Nd = 0.512950 \pm 0.000143$ [2σ]; $^{176}Hf/^{177}Hf = 0.283100 \pm 0.000125$; $^{87}Sr/^{86}Sr = 0.70330 \pm 0.00058$) (33) (Fig. 1). In detail, the depleted kimberlite source overlaps with the geochemically enriched side of the PREMA field, which may be consistent with the lower melting degree of kimberlites and hence, their sampling of more geochemically enriched components compared with OIBs; this is because geochemically enriched material is assumed to be more fusible and is hence preferentially sampled relative to less fusible (i.e., geochemically depleted) materials at lower degrees of melting. Regardless, the data show that, like OIBs, kimberlites sample a ubiquitous PREMA component in Earth's mantle, not a component with primitive $^{143}Nd/^{144}Nd$ and $^{176}Hf/^{177}Hf$ (19).

This observation provides insights into the origin of PREMA. If PREMA compositions are widespread in kimberlites since ~2.06 Ga and in juvenile continental magmas since the Late Archean as previously reported by Stein and Hofmann (14), it seems a fortuitous coincidence that mixing of depleted and enriched mantle components in an evolving Earth can consistently generate such a remarkably homogeneous isotopic composition over geologic time. This is because the composition of subducted crustal material has undoubtedly changed throughout the last 2 billion years—e.g., progressive modification of ocean chemistry and marine sediments (34, 35) and widespread occurrence of mud rocks only in the Phanerozoic due to evolution of vegetation (36). Likewise, the pressure and temperature conditions of metamorphism in subduction zones have also changed significantly throughout Earth history (37). The temperature and oxygen fugacity of the mantle have decreased (38) and increased (39) over time, respectively, which is reflected by the composition of mafic magmas through time (40). Given radical changes in subduction conditions and subducted protolith compositions, it is unlikely that subducted crust, when mixed with depleted mantle such as the MORB source, gives rise to the relatively narrow range of PREMA-like compositions consistently through time. This supports a hypothesis where PREMA is a long-lived primordial mantle domain, not a mixture of geochemically enriched and geochemically depleted domains.

The linear isotopic evolution of kimberlites through time (Fig. 2) allows us to extrapolate the composition of the geochemically depleted PREMA domain back in time and estimate its initial composition. Projection of the $^{143}Nd/^{144}Nd$ and $^{176}Hf/^{177}Hf$ isotope evolution of the depleted kimberlite source to the approximate age of Earth formation (4.567 Ga) returns initial $^{143}Nd/^{144}Nd$ and $^{176}Hf/^{177}Hf$ values of 0.50657 ± 0.00010 (1σ) and 0.27983 ± 0.00012, respectively, which are within uncertainty of chondrite initial values [$^{143}Nd/^{144}Nd = 0.50669 \pm 0.00004$; $^{176}Hf/^{177}Hf = 0.27979 \pm 0.00001$ (41)]. If this extrapolation is valid, the kimberlite $^{143}Nd/^{144}Nd$ and $^{176}Hf/^{177}Hf$ data suggest that the PREMA domain, sampled by OIBs today and kimberlites over the past >2 billion years, could have been established not long after after Earth's accretion from chondritic material. Critically, however, the calculated $^{147}Sm/^{144}Nd$ (0.2086 ± 0.0022; 1σ) and $^{176}Lu/^{177}Hf$ (0.0358 ± 0.0010) ratios of the PREMA domain tapped by kimberlites must be suprachondritic to generate the geochemically depleted (i.e., high) $^{143}Nd/^{144}Nd$ and $^{176}Hf/^{177}Hf$ isotopic compositions that characterize PREMA. Hence, kimberlites do not sample a primitive, circa-chondritic mantle reservoir as previously suggested (19) but rather, a domain (PREMA), which derived from early depletion of chondritic mantle.

These Sm/Nd and Lu/Hf ratios are remarkably similar to those of the Early Depleted Reservoir (EDR) modeled by Caro and Bourdon (42) (referred to as "Super-Chondritic Earth Model" in their paper). The EDR was originally conceived as the portion of mantle that experienced differentiation via silicate melt extraction within the first 30 My of Earth accretion, leaving behind an early geochemically depleted silicate reservoir with elevated (suprachondritic) Sm/Nd that evolved to higher than chondritic

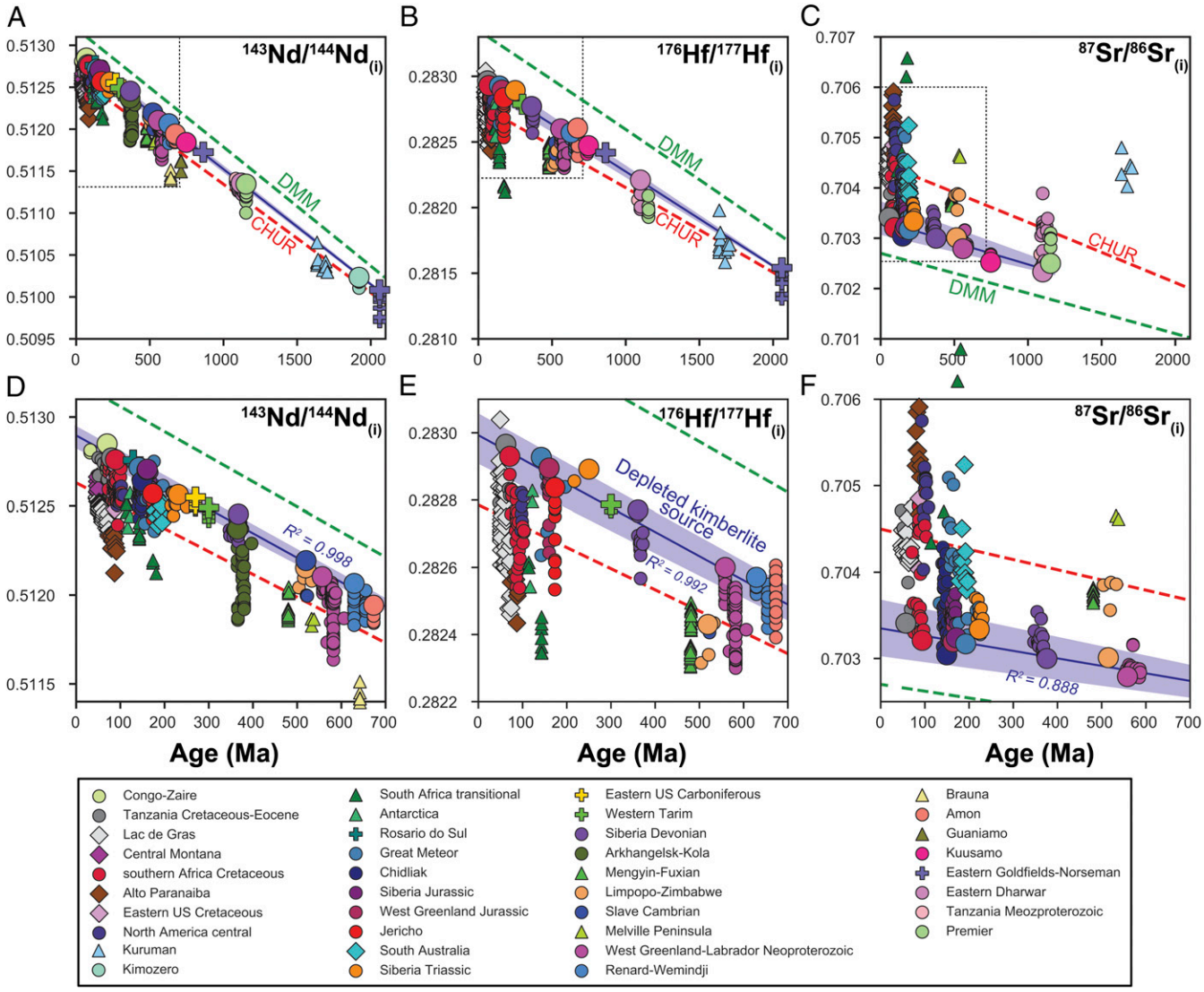

Fig. 2. Nd, Hf, and Sr isotope evolution of kimberlites and ultramafic lamprophyres through time. (*A*) $^{143}Nd/^{144}Nd$ vs. time, (*B*) $^{176}Hf/^{177}Hf$ vs. time, and (*C*) $^{87}Sr/^{86}Sr$ vs. time. *D–F* show the last 700 My of isotopic evolution for the Nd, Hf, and Sr isotope systems, respectively. All of the isotopic ratios represent initial values corrected for radiogenic ingrowth using the emplacement ages of kimberlites and ultramafic lamprophyres. The evolution of the depleted kimberlite source (dark blue lines with 2σ uncertainty envelope in lighter blue) represents a linear regression through the most radiogenic $^{143}Nd/^{144}Nd$ and $^{176}Hf/^{177}Hf$ values and least radiogenic $^{87}Sr/^{86}Sr$ ratios (i.e., larger symbols) of kimberlites (circles) and ultramafic lamprophyres (crosses) from each province (Dataset S2). The provinces that contain geochemically enriched kimberlites (diamonds) and transitional kimberlites (triangles) are excluded from these regressions because their isotopic compositions are dominated by recycled subducted and/or enriched lithospheric components (19, 26, 31). Three kimberlite provinces are also excluded from the regressions in $^{176}Hf/^{177}Hf$ vs. time charts (i.e., Limpopo–Zimbabwe, Premier, Slave–Cambrian) because their $^{176}Hf/^{177}Hf$ ratios are all moderately to highly unradiogenic probably due to the ubiquitous alteration of kimberlites from these provinces. All age and Nd-Hf-Sr isotopic values are reported in Dataset S1. *Materials and Methods* show the values employed to calculate the isotopic evolutions of the DMM and CHUR.

$^{143}Nd/^{144}Nd$. This early silicate differentiation occurred during the lifetime of the short-lived isotope ^{146}Sm (i.e., first 500 Ma of Earth's history), and due to the decay of ^{146}Sm to ^{142}Nd (half-life ~ 103 My), the elevated Sm/Nd in the EDR also yields anomalously high $^{142}Nd/^{144}Nd$ in the accessible Earth (relative to certain classes of chondrites) (43). A complementary hidden enriched reservoir with low Sm/Nd, low $^{143}Nd/^{144}Nd$, and low $^{142}Nd/^{144}Nd$ is also predicted by this model but has not yet been observed. In this model, continental crust was subsequently extracted from the EDR, thereby generating the depleted mantle source of MORB, explaining why MORBs and OIBs (which sample recycled crust) exhibit anomalously high $^{142}Nd/^{144}Nd$ compared to most chondrites. However, while this $^{142}Nd/^{144}Nd$ difference was interpreted to signal an early terrestrial silicate differentiation event (43), later work attributed the elevated $^{142}Nd/^{144}Nd$ in the accessible silicate Earth to poor mixing of nucleosynthetic heterogeneities during solar system formation—where the Earth formed from a region of the solar nebula with higher $^{142}Nd/^{144}Nd$ than most chondrites—rather than radioactive decay (44, 45). As a result, the existence of the EDR has been questioned.

Nonetheless, up to 10 ppm of the $^{142}Nd/^{144}Nd$ difference between Earth and enstatite chondrites (44–46) (i.e., the chondrites with isotopic compositions most similar to Earth) may be the result of ^{146}Sm decay [discussion is in de Leeuw et al. (47) and Willhite et al. (48)]. Therefore, the $^{142}Nd/^{144}Nd$ difference between Earth and enstatite chondrites can be explained as the result of marginally suprachondritic Sm/Nd in the accessible Earth. In this model, the required Sm/Nd is sufficiently high to

generate the suprachondritic $^{143}Nd/^{144}Nd$ observed in PREMA domains (48). Alternatively, if $^{142}Nd/^{144}Nd$ differences between Earth and chondrites reflect purely nucleosynthetic processes, then early formation of PREMA and its long-term suprachondritic $^{143}Nd/^{144}Nd$ composition could still be explained if Earth differentiation by silicate melt extraction and development of suprachondritic Sm/Nd was delayed until the abundance of short-lived ^{146}Sm had been greatly diminished by decay. For example, if the Moon-forming impact at ∼4.45 to 4.40 Ga (49) triggered the global silicate differentiation event, which generated an early-formed depleted domain (50) and hence, PREMA, this delayed early differentiation event would not generate observable positive $^{142}Nd/^{144}Nd$ anomalies in the depleted silicate Earth. In detail, the Sm/Nd ratio required to generate the present-day (kimberlite-based) PREMA $^{143}Nd/^{144}Nd$ (i.e., $\varepsilon^{143}Nd$ of +5.2) from differentiation of a chondritic mantle at ∼4.40 to 4.45 Ga would generate only a small $^{142}Nd/^{144}Nd$ anomaly of a magnitude that is close to the external reproducibility of modern instruments (i.e., 5 ppm) and would be difficult to resolve analytically (47,50). An even later silicate differentiation event (i.e., not linked to lunar formation) would further suppress generation of resolvable $^{142}Nd/^{144}Nd$ anomalies while permitting formation of the suprachondritic $^{143}Nd/^{144}Nd$ observed in PREMA. This might explain the lack of resolvable $^{142}Nd/^{144}Nd$ anomalies in previously analyzed kimberlites (43). Hence, it is possible that PREMA represents a portion of an early depleted mantle domain that has not been modified since Early Hadean silicate Earth differentiation (51), and the isotopic compositions of kimberlites are best explained by episodic tapping of this PREMA composition over geologic time. An ancient origin for PREMA by silicate melt extraction would reconcile the apparently paradoxical association between primordial noble gas compositions, including elevated $^{3}He/^{4}He$ ratios, and $^{143}Nd/^{144}Nd$-$^{176}Hf/^{177}Hf$ ratios indicative of long-term depletion in the PREMA domain sampled by OIBs.

Early Earth Remnants above the Core–Mantle Boundary

Survival of a minimally modified portion of this early depleted mantle domain (i.e., PREMA) since shortly after Earth accretion requires (partial) isolation from convecting mixing, which is most readily achieved if this domain is located in the deep mantle where convective motions are slowed due to higher viscosity. This hypothesis might be supported by the observation that plumes generating most Phanerozoic kimberlites and modern volcanic hot spots, including OIBs, are dominantly sourced from large seismically anomalous regions (i.e., LLSVPs) above the core–mantle boundary (20, 52). However, not all kimberlites are linked to the LLSVPs, and it is unknown if the geochemistry of kimberlites (i.e., PREMA compositions) varies as a function of their geographic relationship with the LLSVPs. To constrain whether PREMA-like kimberlites were spatially correlated with the LLSVPs at the time of their eruption, we have examined the geographic distribution of kimberlites and related ultramafic lamprophyres for which Sr-Nd-Hf isotope compositions are available. This survey is limited to the last ∼270 Ma, a time interval for which the assumption of LLSVP fixity (53, 54) and the association between LLSVP and plumes from the core–mantle boundary seem to be well constrained (20, 52). Fig. 3 demonstrates that kimberlites with radiogenic isotope compositions typical of PREMA are exclusively associated with the LLSVPs, whereas kimberlites that lack a PREMA signature occur both above and far away from the LLSVPs. This observation supports the hypothesis that minimally modified remnants of early Earth differentiation are located within these seismically anomalous regions representing thermochemical piles above the core–mantle boundary and is consistent with the elevated (primordial) $^{3}He/^{4}He$ ratio of OIBs sourced from mantle plumes rooted into the LLSVPs (8).

In conclusion, this study demonstrates that kimberlites and ultramafic lamprophyres as old as 2.1 Ga sample a similar PREMA component as that occurring in OIBs and that this component likely represents a remnant of early Earth differentiation. This can explain the association of primordial noble gas signatures in kimberlites and OIBs with Nd-Hf isotope

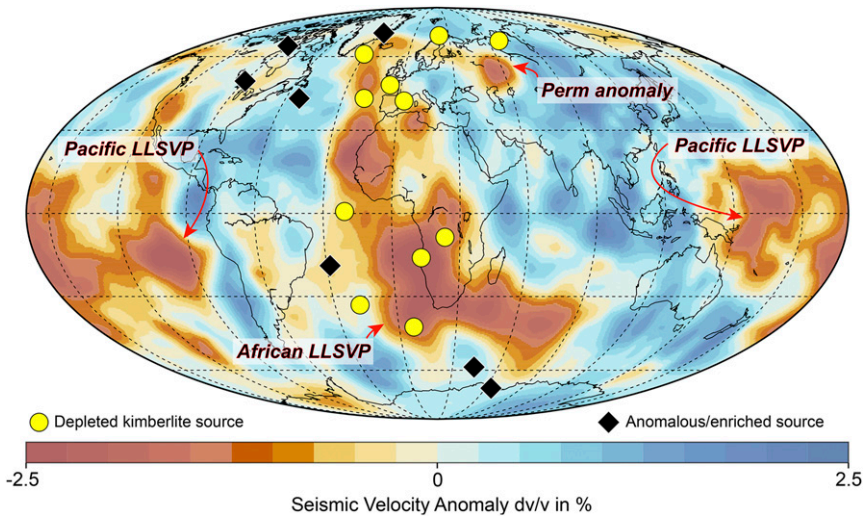

Fig. 3. Geographic distribution of the depleted kimberlite source (PREMA) in Earth's mantle. Kimberlite and ultramafic lamprophyre provinces within the last 270 My and with available Sr-Nd-Hf isotope compositions are reconstructed to their location at time of eruption and compared with the position of LLSVPs above the core mantle boundary using the GPlates software (78) paired with the continent rotation model of Torsvik et al. (54). LLSVPs are defined based on the 1% (±0.5%; dv/v: shear-wave velocity variation) slow contour of the Savani tomography model (79) at a depth of ∼2,800 km. Kimberlites and ultramafic lamprophyres containing the PREMA component (yellow circles) overlap the LLSVPs at time of eruption, with the notable exception of Siberian Jurassic kimberlites, which are proximal to the Perm low shear-wave anomaly above the core–mantle boundary (80). Conversely, kimberlites lacking the PREMA component (black diamonds) do not exhibit any preferential geographical association with the LLSVPs. These results are independent of the employed seismic tomography model as shown in *SI Appendix*, Fig. S11.

compositions indicative of long-term depletion. Derivation of kimberlites and OIBs from common deep sources is supported not only by the common PREMA contribution to both magma types but also, the occurrence of similar enriched components in OIBs and kimberlites younger than 200 Ma, including EM-1 (*SI Appendix*, Fig. S7) and HIMU (i.e., high U/Pb-type) compositions (55). Although no EM-2 (enriched mantle type-2) compositions have so far been observed in kimberlites, it should be noted that EM-2 OIBs are restricted to the Pacific LLSVP (56), whereas no kimberlites of Mesozoic or younger age were located above the Pacific LLSVP at the time of eruption (20). The exclusive association of PREMA-like kimberlites in the last ∼270 Ma with the LLSVPs suggests that this early Earth component is stored in the LLSVPs, and therefore, the origin of these structures could date back to the time of early Earth differentiation (57). Additional studies of Paleoproterozoic and Archean alkaline ultramafic magmas will be required to augment the isotopic record of kimberlites and ultramafic lamprophyres presented herein, thus improving available constraints on the evolution of the deep mantle in the first half of Earth evolution. Kimberlites hold unique clues of early Earth differentiation, and future examination of their noble gas, ^{182}W, and ^{142}Nd isotope systematics is likely to yield fundamental insights into the evolution and dynamics of Earth's mantle.

Materials and Methods

Database. The initial dataset includes bulk sample $^{143}Nd/^{144}Nd$ and $^{176}Hf/^{177}Hf$ and perovskite $^{87}Sr/^{86}Sr$ isotope compositions for rocks that were labeled kimberlites or carbonate-rich ultramafic lamprophyres (dominantly aillikites) in the original publications. Carbonate-rich ultramafic lamprophyres have similar mineralogical and geochemical compositions to kimberlites, including radiogenic isotope systematics (24, 25, 58–61). The similarity is such that some of these lamprophyres were incorrectly classified as kimberlites when they were originally reported (see below). In this study, kimberlites and carbonate-rich ultramafic lamprophyres are considered to be derived from similar sources even though we recognize that the actual petrogenetic relationship between these magmas is unclear. In this compilation, we do not consider group II kimberlites, subsequently renamed orangeites (62) and more recently, African or Kaapvaal lamproites (63), because these rocks represent carbonate-rich olivine lamproites derived from metasomatized (i.e., geochemically enriched) lithospheric mantle sources (24, 32, 64). The database consists of 817 kimberlite and ultramafic lamprophyre samples from localities worldwide (*SI Appendix*, Fig. S1), all associated with a robust age, including 752 whole-rock and perovskite $^{143}Nd/^{144}Nd$ compositions, 432 whole-rock $^{176}Hf/^{177}Hf$ values, and 288 perovskite $^{87}Sr/^{86}Sr$ ratios (Dataset S1).

Lithological Screening. Different rock types have been described as kimberlites in the literature, largely due to the economic implications that the term kimberlite bears for diamond exploration and the fact that most of these bodies were discovered by diamond prospectors. Therefore, we have reevaluated previous classifications of kimberlites for which radiogenic isotope data are available based on mineralogical and geochemical information from the literature, and our preferred classification is reported in Datasets S1 and S3. The following petrographic criteria have been employed to screen (archetypal) kimberlites from mineralogically similar rocks (i.e., transitional kimberlites, olivine lamproites, and ultramafic lamprophyres) (27): 1) clinopyroxene and melilite are absent in the groundmass of kimberlites; 2) high contents of mica are atypical in the groundmass of kimberlites; and 3) samples that combine compositional evolution of phlogopite mica toward either tetraferriphlogopite or elevated Ti concentrations and spinel following "compositional Trend 2" of Mitchell (65) are not considered to be kimberlites. These rocks have been reclassified as either transitional kimberlites or ultramafic lamprophyres depending on their petrographic and mineral chemical features following the criteria outlined in Mitchell (62) and Tappe et al. (66). Dataset S3 provides a list of the provinces for which a different classification has been adopted compared with that published elsewhere, including the reasons why a revised classification is warranted. These provinces include Kuruman, South Africa (transitional kimberlites); Rosario do Sul, Brazil (ultramafic lamprophyres; i.e., alnoites); western Tarim, China (ultramafic lamprophyres; i.e., aillikites); eastern Goldfields, Australia (ultramafic lamprophyres; i.e., aillikites); and South Australia (kimberlites and aillikites).

For the other samples, we have followed previously published classifications as (archetypal) kimberlites, transitional kimberlites (e.g., South Africa transitional, Brauna–Guaniamo, Antarctica), or ultramafic lamprophyres (e.g., Labrador, eastern United States–Carboniferous). Finally, the eastern Dharwar province in India contains samples that were previously classified as kimberlites, transitional kimberlites, and lamproites (67–70); however, their radiogenic isotope compositions are largely indistinguishable regardless of the considered lithology (except for marginally more radiogenic $^{87}Sr/^{86}Sr$ in samples from the Narayanpet field) (Dataset S1). These samples are, therefore, all included in the final database and treated as a single group.

Transitional kimberlites (and lamproites) contain a dominant contribution from geochemically enriched lithospheric mantle sources. These rocks have been screened out from the statistical treatment of data (see next sections) because our aim is to isolate the sublithospheric (i.e., convecting) mantle source signature of kimberlites and related carbonate-rich ultramafic lamprophyres. Archetypal kimberlites and ultramafic lamprophyres can also contain components derived from enriched lithospheric mantle (25, 31). However, by considering the most radiogenic $^{143}Nd/^{144}Nd$ and $^{176}Hf/^{177}Hf$ and least radiogenic $^{87}Sr/^{86}Sr$ values in each province, these contributions can be filtered out (see below).

Filtering for Crustal Contamination. Kimberlites are hybrid rocks that contain crustal and mantle-derived fragments (i.e., xenoliths) and hydrothermal phases that are not magmatic in origin (27). The issue of crustal contamination is especially problematic for radiogenic isotope studies of kimberlites as shown, for example, by the commonly higher $^{87}Sr/^{86}Sr$ ratios of bulk kimberlite samples compared with those of perovskite, a robust magmatic phase (24, 30, 71). To mitigate this issue, the $^{87}Sr/^{86}Sr$ isotope data we have considered herein are restricted to analyses of perovskite. Even though kimberlite magmas are highly enriched in Nd and to a lesser extent, Hf compared with crustal rocks (24, 28, 29), crustal contamination can also affect the $^{143}Nd/^{144}Nd$ and $^{176}Hf/^{177}Hf$ isotope compositions of bulk kimberlite samples (26, 30). For this reason, we have applied several filters based on major and trace element ratios (Si/Al, Nb/Th, Nb/U, Ba/Nb, Ba/Th, Rb/Th, Ce/Pb, Yb/Gd), which are sensitive to crustal contamination based on previous studies of kimberlite and mafic magmas (28, 29, 48). For each filter, the major or trace element ratios of the primitive mantle (72) and continental crust (73) were first calculated. Next, bins were assigned for values above the larger and below the smaller values of the two aforementioned end-members (i.e., primitive mantle and continental crust); finally, further bins were determined by splitting the difference between the two end-members into evenly sized bins, typically five. Kimberlite and ultramafic lamprophyre samples (for which bulk sample major and/or trace element results were available together with Nd and/or Hf isotope compositions) in the entire database were placed into these bins according to their bulk major and trace element compositions (*SI Appendix*, Figs. S2–S6).

We observe no correlation between major or trace element ratios and Nd or Hf isotope compositions on a global scale (*SI Appendix*, Figs. S2 and S3) or in individual provinces (e.g., southern Africa Cretaceous, Lac de Gras) (*SI Appendix*, Figs. S4–S6). This observation is not unexpected because a range of magmatic, mantle, and crustal components contributes to the bulk compositions of kimberlites. Given that this approach of screening for crustal contamination did not produce appreciable results, we have adopted a different strategy as outlined in the next section.

Filtering for Lithospheric Contribution. In the following, a kimberlite "province" is considered to include one or more clusters and/or fields of kimberlites (and/or ultramafic lamprophyres) from the same geographic region, which were emplaced in a restricted time window (typically <50 My). Kimberlites in each province can, therefore, be traced back to the same source region in the sublithospheric mantle. To understand the source of isotopic variability in each province, we have only considered provinces for which at least three analyses of kimberlites or carbonate-rich ultramafic lamprophyres are available for at least one of the three isotopic systems examined herein.

In most provinces, kimberlites show variable radiogenic isotope compositions despite their similar emplacement ages (Fig. 2 and *SI Appendix*, Figs. S8 and S9). This variability can be attributed to one or more of the following: 1) source heterogeneity in the sublithospheric mantle, most likely related to recycling of subducted or delaminated lithospheric material (19, 26); 2) incorporation of enriched lithospheric mantle material during magma ascent (25, 31); and 3) crustal contamination (26, 30). The common effect of these processes is to decrease $^{143}Nd/^{144}Nd$ and $^{176}Hf/^{177}Hf$, and increase $^{87}Sr/^{86}Sr$ ratios in kimberlites. Textbook examples of the geochemical consequences of these processes include the aillikite dykes at Torngat, Labrador [whose Nd and Hf isotopic compositions form a linear trend from moderately high to

low values attributed to increasing contribution from metasomatized lithospheric mantle (25)] and the Premier kimberlite in South Africa [where $^{143}Nd/^{144}Nd$ in bulk samples is inversely correlated with SiO_2 contents due to increasing crustal contamination (30)]. Therefore, to screen the dataset from the effects of any lithospheric contribution, be it crustal or enriched lithospheric mantle, we have only considered the most radiogenic $^{143}Nd/^{144}Nd$ and $^{176}Hf/^{177}Hf$, and least radiogenic $^{87}Sr/^{86}Sr$ values in each kimberlite province. Commonly, the selected analyses with most radiogenic $^{143}Nd/^{144}Nd$ do not correspond to the most radiogenic $^{176}Hf/^{177}Hf$ ratio for the same kimberlite province because 1) there are considerably more Nd isotope than Hf isotope analyses available, and some Nd isotope compositions are of perovskite separates, which do not have associated Hf isotope ratios, and 2) Nd isotopes in bulk kimberlite samples are more resistant to crustal or lithospheric mantle contamination than Hf isotopes, which results in occasional decoupling between these two isotopic systems in bulk kimberlite rocks. We acknowledge that this approach can also filter out the potential contributions of deeply subducted material in the kimberlite sources. However, our aim is to address the origin of the moderately depleted mantle component, least influenced by crustal recycling processes, that is evident in the majority of kimberlites worldwide (large symbols in Fig. 2). In this sense, some kimberlites appear to be anomalous because they apparently lack this depleted component (see below), or the component exists but the appropriate samples have not been analyzed.

Screening of Geochemically Enriched Kimberlites. The transitional kimberlites identified above based on petrographic and mineral chemical criteria typically feature geochemically enriched isotopic signatures (i.e., moderately to strongly unradiogenic $^{143}Nd/^{144}Nd$ and $^{176}Hf/^{177}Hf$ ratios combined with moderate to high $^{87}Sr/^{86}Sr$ values) (triangles in Fig. 2). Kimberlites from four "young" (i.e., <200-My) provinces (Lac de Gras and North America Central Corridor in Canada, Alto Paranaiba in Brazil, and South Australia) exhibit $^{87}Sr/^{86}Sr$ ratios that are moderately (Lac de Gras, South Australia) to strongly radiogenic (North America Central Corridor, Alto Paranaiba) and never extend to the unradiogenic compositions of kimberlites elsewhere with similar ages (diamonds in Fig. 2). However, these geochemically enriched kimberlites do not exhibit mineralogical or mineral chemical features of transitional kimberlites. They are located in proximity of the paleomargins of Pangea, and their sources were probably enriched by subduction of oceanic lithosphere in the convecting mantle (19, 26) as also indicated by studies of sublithospheric diamonds in other Cretaceous kimberlites from Brazil (74, 75). Kimberlites with such geochemical characteristics are not commonly observed prior to 200 My, perhaps due to limited contribution of recycled lithospheric material to the deep source of kimberlites (19). As the aim of this work is to identify the long-term evolution of the depleted component in the kimberlite sources, samples from these four provinces have been screened out from calculation of the long-term $^{143}Nd/^{144}Nd$ and $^{176}Hf/^{177}Hf$ kimberlite source composition (but are shown in the figures to provide important context). While other provinces also include kimberlites with moderately radiogenic $^{87}Sr/^{86}Sr$ ratios (e.g., southern Africa Cretaceous, Great Meteor) (Fig. 2), some kimberlites from these provinces show isotopically depleted compositions, which are here considered to be representative of the depleted mantle component occurring in the majority of kimberlites worldwide. Hence, these provinces have been retained in the calculations below.

Statistical Treatment of Data. To understand the present-day composition of the deep kimberlite source (i.e., its depleted component) and its evolution with time, we have calculated linear regressions through the most radiogenic $^{143}Nd/^{144}Nd$ and $^{176}Hf/^{177}Hf$, and least radiogenic $^{87}Sr/^{86}Sr$ ratios in $^{143}Nd/^{144}Nd$, $^{176}Hf/^{177}Hf$, and $^{87}Sr/^{86}Sr$ vs. time charts (Fig. 2 and *SI Appendix*, Fig. S10). These regressions allow derivation of present-day $^{143}Nd/^{144}Nd$, $^{176}Hf/^{177}Hf$, and $^{87}Sr/^{86}Sr$ values as well as time-integrated $^{147}Sm/^{144}Nd$, $^{176}Lu/^{177}Hf$, and $^{87}Rb/^{86}Sr$ ratios in the kimberlite source least influenced by recycled crustal material.

We employed four different methods for calculating linear regressions using the Python programming language ("numpy.polyfit," "smols," "scipy.stats.linregress," and "np.linalg.lstsq"). These functions calculate a least squares polynomial or linear fit through the data and attempts to minimize the squared errors from the regression. Outputs also include the covariances of both the gradient and the *y* intercept. The results of these calculations are broadly similar, and those from polyfit and linregress are compared in *SI Appendix*, Fig. S10. All of the data points were included in the linear regressions calculated for $^{143}Nd/^{144}Nd$ vs. age and $^{87}Sr/^{86}Sr$ vs. age, whereas three low-$^{176}Hf/^{177}Hf$ data points (Limpopo–Zimbabwe, Premier, Slave–Cambrian) were removed from the $^{176}Hf/^{177}Hf$ vs. age regression because they fell outside the 2σ envelope of the regression. The majority of kimberlites in these provinces are altered, which suggests that the depleted Hf component of these kimberlites could not be correctly identified. Nonetheless, inclusion of these results would not alter the output of this model but rather, generate considerably larger uncertainties (e.g., present-day $^{176}Hf/^{177}Hf = 0.282993 \pm 0.000156$ [2σ] compared with 0.283013 ± 0.000076 when the outliers are removed).

The apparently robust correlations between age and isotopic compositions in Fig. 2 (i.e., $R^2 = 0.998$, 0.993, and 0.882 for Nd, Hf, and Sr isotopes, respectively) were then subjected to the standard two-tailed Student's *t* test for the null hypothesis that the correlations between variables occur by chance. We calculated *t* values at the 99% level of confidence using the relationship $t = r \times \sqrt{\frac{n-2}{1-r^2}}$, where *n* is the number of data points and *r* is the correlation coefficient. None of the correlations examined are likely to have occurred by chance because calculated *t* values are significantly higher than critical *t* values [i.e., Nd isotopes: $n = 26$, $t_{calc} = 109 >> t_{crit\ (0.01;\ 26)} = 3.7$; Hf isotopes: $n = 15$, $t_{calc} = 43 >> t_{crit\ (0.01;\ 15)} = 4.1$; Sr isotopes: $n = 13$, $t_{calc} = 9.1 >> t_{crit\ (0.01;\ 13)} = 4.2$]. The regression results generated using linregress are reported in Fig. 2 and have been employed for modeling the origin and evolution of the kimberlite source, including its present-day composition.

Linear regression models were also run on Minitab 19 with the Predict function used to extrapolate the initial $^{143}Nd/^{144}Nd$ and $^{176}Hf/^{177}Hf$ compositions of the kimberlite source to 4.567 Ga. This software was also employed to determine the uncertainties of the initial values based on the confidence and prediction intervals of the regression model.

Comparison with Other Geochemical Reservoirs. The present-day isotopic composition of the kimberlite source obtained from the regressions above is compared with the compositions of other mantle end-members (e.g., DMM, PREMA, or FOZO) in Fig. 1. The present-day $^{143}Nd/^{144}Nd$ and $^{87}Sr/^{86}Sr$ composition of PREMA is taken from Konter et al. (33), whose Geochemical Centre represents the volume where the trends formed by each ocean island chain converge in Sr-Nd-Pb isotope space. The PREMA $^{176}Hf/^{177}Hf$ ratio (and 2σ variability) is then calculated using the Geochemical Centre $^{143}Nd/^{144}Nd$ value and the Nd-Hf mantle array of Chauvel et al. (76). This comparison shows that the present-day isotopic composition of the depleted kimberlite source is indistinguishable from the OIB-based PREMA (Fig. 1).

In Fig. 2, the isotopic evolution of the DMM with time is calculated following the method of Stracke et al. (77) and assuming differentiation occurred at ∼4.4 Ga. We employed present-day DMM values of 0.51320 for $^{143}Nd/^{144}Nd$, 0.28335 for $^{176}Hf/^{177}Hf$, and 0.70270 for $^{87}Sr/^{86}Sr$. For the Nd-Hf isotope evolution of the Chondrite Uniform Reservoir (CHUR), we employed the model of Bouvier et al. (41), while for Sr isotopes, we used the following values: $^{87}Sr/^{86}Sr_{present\ day} = 0.7045$ and $^{87}Rb/^{86}Sr = 0.0827$.

Finally, the initial $^{143}Nd/^{144}Nd$ and $^{176}Hf/^{177}Hf$ compositions of the kimberlite source at 4.567 Ga calculated using linregress and Predict (see above) were compared with the initial CHUR composition of Bouvier et al. (41): $^{143}Nd/^{144}Nd_{kimberlite\text{-}source,4.567Ga}$ (linregress) $= 0.50657 \pm 0.00010$ (1σ), $^{143}Nd/^{144}Nd_{kimberlite\text{-}source,4.567Ga}$ (Predict) $= 0.50663 \pm 0.00005$, $^{143}Nd/^{144}Nd_{CHUR,4.567Ga} = 0.50669 \pm 0.00004$; and $^{176}Hf/^{177}Hf_{kimberlite\text{-}source,4.567Ga}$ (linregress) $= 0.27983 \pm 0.00012$, $^{176}Hf/^{177}Hf_{kimberlite\text{-}source,4.567Ga}$ (Predict) $= 0.27978 \pm 0.00007$, $^{176}Hf/^{177}Hf_{CHUR} = 0.27979 \pm 0.00001$. These results indicate that the $^{143}Nd/^{144}Nd$ and $^{176}Hf/^{177}Hf$ compositions of the depleted kimberlite source are within uncertainty of CHUR values at the approximate time of Earth formation and suggest that the depleted kimberlite source derived from differentiation of a mantle with chondritic composition via silicate melt extraction not long after Earth accretion.

Data Availability. All study data are included in the article and supporting information.

ACKNOWLEDGMENTS. We thank Jon Woodhead, Janet Hergt, Rick Carlson, Paolo Sossi, Brad Peters, and Andreas Stracke for discussions and Matteo Desiderio for proofreading this manuscript. Comments from the editor and two anonymous reviewers have improved the clarity of this contribution. This research was funded by Swiss National Science Foundation Ambizione Fellowship PZ00P2_180126/1 (to A.G.) and NSF Grant NSF EAR-1900652 (to M.G.J.).

1. R. Montelli, G. Nolet, F. A. Dahlen, G. Masters, A catalogue of deep mantle plumes: New results from finite-frequency tomography. *Geochem. Geophys. Geosyst.* **7**, Q11007 (2006).
2. S. W. French, B. Romanowicz, Broad plumes rooted at the base of the Earth's mantle beneath major hotspots. *Nature* **525**, 95–99 (2015).
3. M. D. Kurz, W. J. Jenkins, S. R. Hart, Helium isotopic systematics of oceanic islands and mantle heterogeneity. *Nature* **297**, 43–47 (1982).
4. S. Mukhopadhyay, R. Parai, Noble gases: A record of Earth's evolution and mantle dynamics. *Annu. Rev. Earth Planet. Sci.* **47**, 389–419 (2019).
5. D. J. DePaolo, Crustal growth and mantle evolution: Inferences from models of element transport and Nd and Sr isotopes. *Geochim. Cosmochim. Acta* **44**, 1185–1196 (1980).
6. A. W. Hofmann, Chemical differentiation of the Earth: The relationship between mantle, continental crust, and oceanic crust. *Earth Planet. Sci. Lett.* **90**, 297–314 (1988).
7. C. G. Macpherson, D. R. Hilton, J. M. Sinton, R. J. Poreda, H. Craig, High 3He/4He ratios in the Manus backarc basin: Implications for mantle mixing and the origin of plumes in the western Pacific Ocean. *Geology* **26**, 1007–1010 (1998).
8. C. D. Williams, S. Mukhopadhyay, M. L. Rudolph, B. Romanowicz, Primitive helium is sourced from seismically slow regions in the lowermost mantle. *Geochem. Geophys. Geosyst.* **20**, 4130–4145 (2019).
9. S. R. Hart, E. H. Hauri, L. A. Oschmann, J. A. Whitehead, Mantle plumes and entrainment: Isotopic evidence. *Science* **256**, 517–520 (1992).
10. A. Zindler, S. Hart, Chemical geodynamics. *Annu. Rev. Earth Planet. Sci.* **14**, 493–571 (1986).
11. A. Stracke, Earth's heterogeneous mantle: A product of convection-driven interaction between crust and mantle. *Chem. Geol.* **330-331**, 274–299 (2012).
12. B. B. Hanan, D. W. Graham, Lead and helium isotope evidence from oceanic basalts for a common deep source of mantle plumes. *Science* **272**, 991–995 (1996).
13. A. Stracke, A. W. Hofmann, S. R. Hart, FOZO, HIMU, and the rest of the mantle zoo. *Geochem. Geophys. Geosyst.* **6**, Q05007 (2005).
14. M. Stein, A. W. Hofmann, Mantle plumes and episodic crustal growth. *Nature* **372**, 63–68 (1994).
15. G. Wörner, A. Zindler, H. Staudigel, H. U. Schmincke, Sr, Nd, and Pb isotope geochemistry of Tertiary and Quaternary alkaline volcanics from West Germany. *Earth Planet. Sci. Lett.* **79**, 107–119 (1986).
16. C. Class, S. L. Goldstein, Evolution of helium isotopes in the Earth's mantle. *Nature* **436**, 1107–1112 (2005).
17. H. Sumino, I. Kaneoka, K. Matsufuji, A. V. Sobolev, Deep mantle origin of kimberlite magmas revealed by neon isotopes. *Geophys. Res. Lett.* **33**, L16318 (2006).
18. Y. Tachibana, I. Kaneoka, A. Gaffney, B. Upton, Ocean-island basalt-like source of kimberlite magmas from West Greenland revealed by high 3He/4He ratios. *Geology* **34**, 273–276 (2006).
19. J. Woodhead *et al*., Kimberlites reveal 2.5-billion-year evolution of a deep, isolated mantle reservoir. *Nature* **573**, 578–581 (2019).
20. T. H. Torsvik, K. Burke, B. Steinberger, S. J. Webb, L. D. Ashwal, Diamonds sampled by plumes from the core-mantle boundary. *Nature* **466**, 352–355 (2010).
21. L. M. Heaman, B. A. Kjarsgaard, Timing of eastern North American kimberlite magmatism: Continental extension of the great meteor hotspot track? *Earth Planet. Sci. Lett.* **178**, 253–268 (2000).
22. L. M. Heaman, D. Phillips, G. Pearson, Dating kimberlites: Methods and emplacement patterns through time. *Elements* **15**, 399–404 (2019).
23. A. Giuliani *et al*., Kimberlite genesis from a common carbonate-rich primary melt modified by lithospheric mantle assimilation. *Sci. Adv.* **6**, eaaz0424 (2020).
24. D. G. Pearson, J. Woodhead, P. E. Janney, Kimberlites as geochemical probes of Earth's mantle. *Elements* **15**, 387–392 (2019).
25. S. Tappe *et al*., Between carbonatite and lamproite—diamondiferous Torngat ultramafic lamprophyres formed by carbonate-fluxed melting of cratonic MARID-type metasomes. *Geochim. Cosmochim. Acta* **72**, 3258–3286 (2008).
26. S. Tappe, G. D. Pearson, B. A. Kjarsgaard, G. Nowell, D. Dowall, Mantle transition zone input to kimberlite magmatism near a subduction zone: Origin of anomalous Nd–Hf isotope systematics at Lac de Gras, Canada. *Earth Planet. Sci. Lett.* **371–372**, 235–251 (2013).
27. R. H. Mitchell, A. Giuliani, H. O'Brien, What is a kimberlite? Petrology and mineralogy of hypabyssal kimberlites. *Elements* **15**, 381–386 (2019).
28. M. Becker, A. P. le Roex, Geochemistry of South African on- and off-craton, group I and group II kimberlites: Petrogenesis and source region evolution. *J. Petrol.* **47**, 673–703 (2006).
29. B. A. Kjarsgaard, D. G. Pearson, S. Tappe, G. M. Nowell, D. P. Dowall, Geochemistry of hypabyssal kimberlites from Lac de Gras, Canada: Comparisons to a global database and applications to the parent magma problem. *Lithos* **112S**, 236–248 (2009).
30. F.-Y. Wu *et al*., In situ U-Pb age determination and Sr-Nd isotopic analysis of perovskite from the Premier (Cullinan) kimberlite, South Africa. *Chem. Geol.* **353**, 83–95 (2013).
31. A. Araujo, R. W. Carlson, J. C. Gaspar, L. A. Bizzi, Petrology of kamafugites and kimberlites from the Alto paranaíba alkaline province, Minas Gerais, Brazil. *Contrib. Mineral. Petrol.* **142**, 163–177 (2001).
32. G. M. Nowell *et al*., Hf isotope systematics of kimberlites and their megacrysts: New constraints on their source regions. *J. Petrol.* **45**, 1583–1612 (2004).
33. J. G. Konter *et al*., One hundred million years of mantle geochemical history suggest the retiring of mantle plumes is premature. *Earth Planet. Sci. Lett.* **275**, 285–295 (2008).
34. P. G. Eriksson *et al*., Secular changes in sedimentation systems and sequence stratigraphy. *Gondwana Res.* **24**, 468–489 (2013).
35. A. Ridgwell, R. E. Zeebe, The role of the global carbonate cycle in the regulation and evolution of the Earth system. *Earth Planet. Sci. Lett.* **234**, 299–315 (2005).
36. W. J. McMahon, N. S. Davies, Evolution of alluvial mudrock forced by early land plants. *Science* **359**, 1022–1024 (2018).
37. R. M. Holder, D. R. Viete, M. Brown, T. E. Johnson, Metamorphism and the evolution of plate tectonics. *Nature* **572**, 378–381 (2019).
38. C. Herzberg, K. Condie, J. Korenaga, Thermal history of the Earth and its petrological expression. *Earth Planet. Sci. Lett.* **292**, 79–88 (2010).
39. S. Aulbach *et al*., Evidence for a dominantly reducing Archaean ambient mantle from two redox proxies, and low oxygen fugacity of deeply subducted oceanic crust. *Sci. Rep.* **9**, 20190 (2019).
40. C. B. Keller, B. Schoene, Statistical geochemistry reveals disruption in secular lithospheric evolution about 2.5 Gyr ago. *Nature* **485**, 490–493 (2012).
41. A. Bouvier, J. D. Vervoort, P. J. Patchett, The Lu-Hf and Sm-Nd isotopic composition of CHUR: Constraints from unequilibrated chondrites and implications for the bulk composition of terrestrial planets. *Earth Planet. Sci. Lett.* **273**, 48–57 (2008).
42. G. Caro, B. Bourdon, Non-chondritic Sm/Nd ratio in the terrestrial planets: Consequences for the geochemical evolution of the mantle–crust system. *Geochim. Cosmochim. Acta* **74**, 3333–3349 (2010).
43. M. Boyet, R. W. Carlson, 142Nd evidence for early (>4.53 Ga) global differentiation of the silicate Earth. *Science* **309**, 576–581 (2005).
44. A. Bouvier, M. Boyet, Primitive solar system materials and Earth share a common initial ^{142}Nd abundance. *Nature* **537**, 399–402 (2016).
45. C. Burkhardt *et al*., A nucleosynthetic origin for the Earth's anomalous ^{142}Nd composition. *Nature* **537**, 394–398 (2016).
46. A. Gannoun, M. Boyet, H. Rizo, A. El Goresy, 146Sm-142Nd systematics measured in enstatite chondrites reveals a heterogeneous distribution of 142Nd in the solar nebula. *Proc. Natl. Acad. Sci. U.S.A.* **108**, 7693–7697 (2011).
47. G. A. M. de Leeuw, R. M. Ellam, F. M. Stuart, R. W. Carlson, 142Nd/144Nd inferences on the nature and origin of the source of high 3He/4He magmas. *Earth Planet. Sci. Lett.* **472**, 62–68 (2017).
48. L. N. Willhite *et al*., Hot and heterogenous high-3He/4He components: New constraints from Proto-Iceland plume lavas from Baffin island. *Geochem. Geophys. Geosyst.* **20**, 5939–5967 (2020).
49. M. Maurice, N. Tosi, S. Schwinger, D. Breuer, T. Kleine, A long-lived magma ocean on a young Moon. *Sci. Adv.* **6**, eaba8949 (2020).
50. R. W. Carlson, M. Garçon, J. O'Neil, J. Reimink, H. Rizo, The nature of Earth's first crust. *Chem. Geol.* **530**, 119321 (2019).
51. M. G. Jackson *et al*., Evidence for the survival of the oldest terrestrial mantle reservoir. *Nature* **466**, 853–856 (2010).
52. K. Burke, B. Steinberger, T. H. Torsvik, M. A. Smethurst, Plume generation zones at the margins of large low shear velocity provinces on the core–mantle boundary. *Earth Planet. Sci. Lett.* **265**, 49–60 (2008).
53. C. P. Conrad, B. Steinberger, T. H. Torsvik, Stability of active mantle upwelling revealed by net characteristics of plate tectonics. *Nature* **498**, 479–482 (2013).
54. T. H. Torsvik *et al*., Deep mantle structure as a reference frame for movements in and on the Earth. *Proc. Natl. Acad. Sci. U.S.A.* **111**, 8735–8740 (2014).
55. K. D. Collerson, Q. Williams, A. E. Ewart, D. T. Murphy, Origin of HIMU and EM-1 domains sampled by ocean island basalts, kimberlites and carbonatites: The role of CO2-fluxed lower mantle melting in thermochemical upwellings. *Phys. Earth Planet. Inter.* **181**, 112–131 (2010).
56. M. G. Jackson, T. W. Becker, J. G. Konter, Geochemistry and distribution of recycled domains in the mantle inferred from Nd and Pb isotopes in oceanic hot spots: Implications for storage in the large low shear wave velocity provinces. *Geochem. Geophys. Geosyst.* **19**, 3496–3519 (2018).
57. S. Labrosse, J. W. Hernlund, N. Coltice, A crystallizing dense magma ocean at the base of the Earth's mantle. *Nature* **450**, 866–869 (2007).
58. H. Dalton *et al*., Petrogenesis of a hybrid cluster of evolved kimberlites and ultramafic lamprophyres in the Kuusamo area, Finland. *J. Petrol.* **60**, 2025–2050 (2020).
59. R. H. Mitchell, B. H. Scott Smith, L. M. Larsen, *Proceedings of the VIIth International Kimberlite Conference*, J. J. Gurney, M. D. Pascoe, S. H. Richardson, Eds. (Red Roof Design, Cape Town, South Africa, 1999), vol. 2, pp. 574-583.
60. C. B. Smith, S. E. Haggerty, B. Chatterjee, A. Beard, R. Townend, Kimberlite, lamproite, ultramafic lamprophyre, and carbonatite relationships on the Dharwar Craton, India; an example from the Khaderpet pipe, a diamondiferous ultramafic with associated carbonatite intrusion. *Lithos* **182-183**, 102–113 (2013).
61. S. Tappe *et al*., Genesis of ultramafic lamprophyres and carbonatites at Aillik Bay, Labrador: A consequence of incipient lithospheric thinning beneath the North Atlantic craton. *J. Petrol.* **47**, 1261–1315 (2006).
62. R. H. Mitchell, *Kimberlites, Orangeites and Related Rocks* (Plenum Press, New York, NY, 1995).
63. B. H. Scott Smith *et al*., *A Glossary of Kimberlite and Related Rocks* (Scott-Smith Petrology Inc., North Vancouver, Canada, 2018).
64. A. Giuliani *et al*., Did diamond-bearing orangeites originate from MARID-veined peridotites in the lithospheric mantle? *Nat. Commun.* **6**, 6837 (2015).
65. R. H. Mitchell, *Kimberlites: Mineralogy, Geochemistry and Petrology* (Plenum Publishing Company, New York, NY, 1986).
66. S. Tappe, S. F. Foley, G. A. Jenner, B. A. Kjarsgaard, Integrating ultramafic lamprophyres into the IUGS classification of igneous rocks: Rationale and implications. *J. Petrol.* **46**, 1893–1900 (2005).
67. N. V. Chalapathi Rao, R. K. Srivastava, Petrology and geochemistry of diamondiferous mesoproterozoic kimberlites from Wajrakarur kimberlite field, Eastern Dharwar craton, southern India: Genesis and constraints on mantle source regions. *Contrib. Mineral. Petrol.* **157**, 245–265 (2009).

68. G. Kaur, M. M. Korakoppa, Fareeduddin, K. L. Pruseth, "Petrology of P-5 and P-13 'kimberlites' from Lattavaram Kimberlite Cluster, Wajrakarur Kimberlite Field, Andhra Pradesh, India: Reclassification as lamproites" in *Proceedings of 10th International Kimberlite Conference*, D. G. Pearson*et al*., Eds. (Springer India, New Delhi, India, 2013), pp. 183–194.
69. C. Paton, J. M. Hergt, J. D. Woodhead, D. Phillips, S. R. Shee, Identifying the asthenospheric component of kimberlite magmas from the Dharwar Craton, India. *Lithos* **112S**, 296–310 (2009).
70. A. M. Shaikh *et al*., The P3 kimberlite and P4 lamproite, Wajrakarur kimberlite field, India: Mineralogy, and major and minor element compositions of olivines as records of their phenocrystic vs xenocrystic origin. *Mineral. Petrol.* **112**, 609–624 (2018).
71. J. Woodhead, J. Hergt, D. Phillips, C. Paton, African kimberlites revisited: In situ Sr-isotope analysis of groundmass perovskite. *Lithos* **112S**, 311–317 (2009).
72. W. F. McDonough, S. S. Sun, The composition of the Earth. *Chem. Geol.* **120**, 223–253 (1995).
73. R. L. Rudnick, S. Gao, "Composition of the continental crust" in *Treatise on Geochemistry. The Crust*, H. D. Turekian, K. K. Holland, Eds. (Elsevier, Oxford, United Kingdom, 2014), vol. 4, pp. 1–51.
74. G. P. Bulanova *et al*., Mineral inclusions in sublithospheric diamonds from collier 4 kimberlite pipe, Juina, Brazil: Subducted protoliths, carbonated melts and primary kimberlite magmatism. *Contrib. Mineral. Petrol.* **160**, 489–510 (2010).
75. B. Harte, S. Richardson, Mineral inclusions in diamonds track the evolution of a Mesozoic subducted slab beneath West Gondwanaland. *Gondwana Res.* **21**, 236–245 (2012).
76. C. Chauvel, E. Lewin, M. Carpentier, N. T. Arndt, J.-C. Marini, Role of recycled oceanic basalt and sediment in generating the Hf-Nd mantle array. *Nat. Geosci.* **1**, 64–67 (2008).
77. A. Stracke, M. Bizimis, V. J. M. Salters, Recycling oceanic crust: Quantitative constraints. *Geochem. Geophys. Geosyst.* **4**, 8003 (2003).
78. R. D. Müller *et al*., GPlates: Building a virtual Earth through deep time. *Geochem. Geophys. Geosyst.* **19**, 2243–2261 (2018).
79. L. Auer, L. Boschi, T. W. Becker, T. Nissen-Meyer, D. Giardini, Savani: A variable resolution whole-mantle model of anisotropic shear velocity variations based on multiple data sets. *J. Geophys. Res. Solid Earth* **119**, 3006–3034 (2014).
80. S. Cottaar, V. Lekic, Morphology of seismically slow lower-mantle structures. *Geophys. J. Int.* **207**, 1122–1136 (2016).

Remnants of early Earth differentiation in the deepest mantle-derived lavas

Andrea Giuliani[1,2,*], Matthew G. Jackson[3], Angus Fitzpayne[1], Hayden Dalton[2]

[1] *Institute of Geochemistry and Petrology, Department of Earth Sciences, ETH Zurich, 8092 Zurich, Switzerland*

[2] *Kimberlites and Diamonds (KiDs), School of Earth Sciences, The University of Melbourne, Parkville, 3010 Victoria, Australia*

[3] *Department of Earth Science, University of California, Santa Barbara, 93106, USA*

Supplementary Information

This supplementary file includes Figures S1 to S11, and a supplementary reference list.

The complete datasets are reported in Tables S1 to S3:

Table S1. Summary of age, Nd, Hf and Sr isotope data for kimberlites and carbonate-rich ultramafic lamprophyres from worldwide localities

Table S2. Summary of initial Sr-Nd-Hf isotope compositions and age values for samples in each province which have been employed to calculate the kimberlite PREMA regressions

Table S3. Lithological classification of the samples employed in this work grouped by province

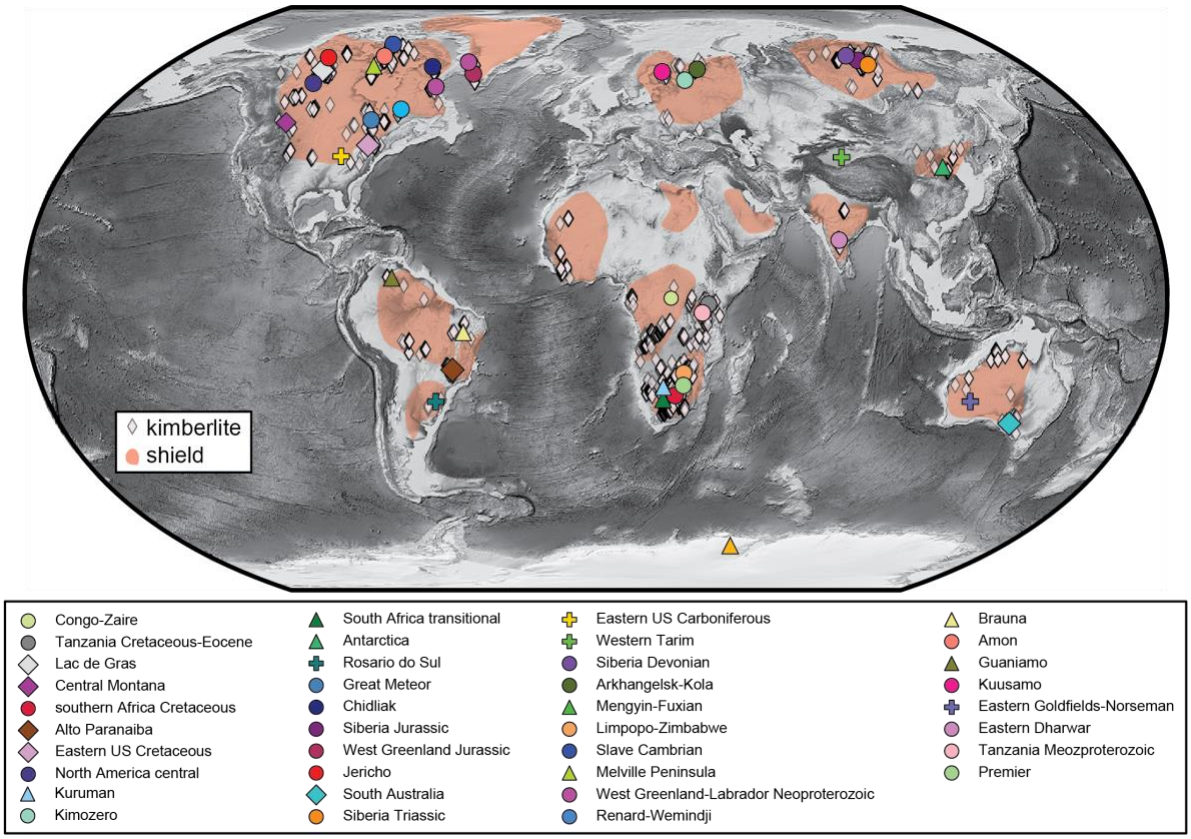

Figure S1. Global elevation map showing the distribution of kimberlite and ultramafic lamprophyre provinces considered in this study. Salmon-coloured fields indicate the positions of continental shields. Map modified from Giuliani and Pearson ***(114)***.

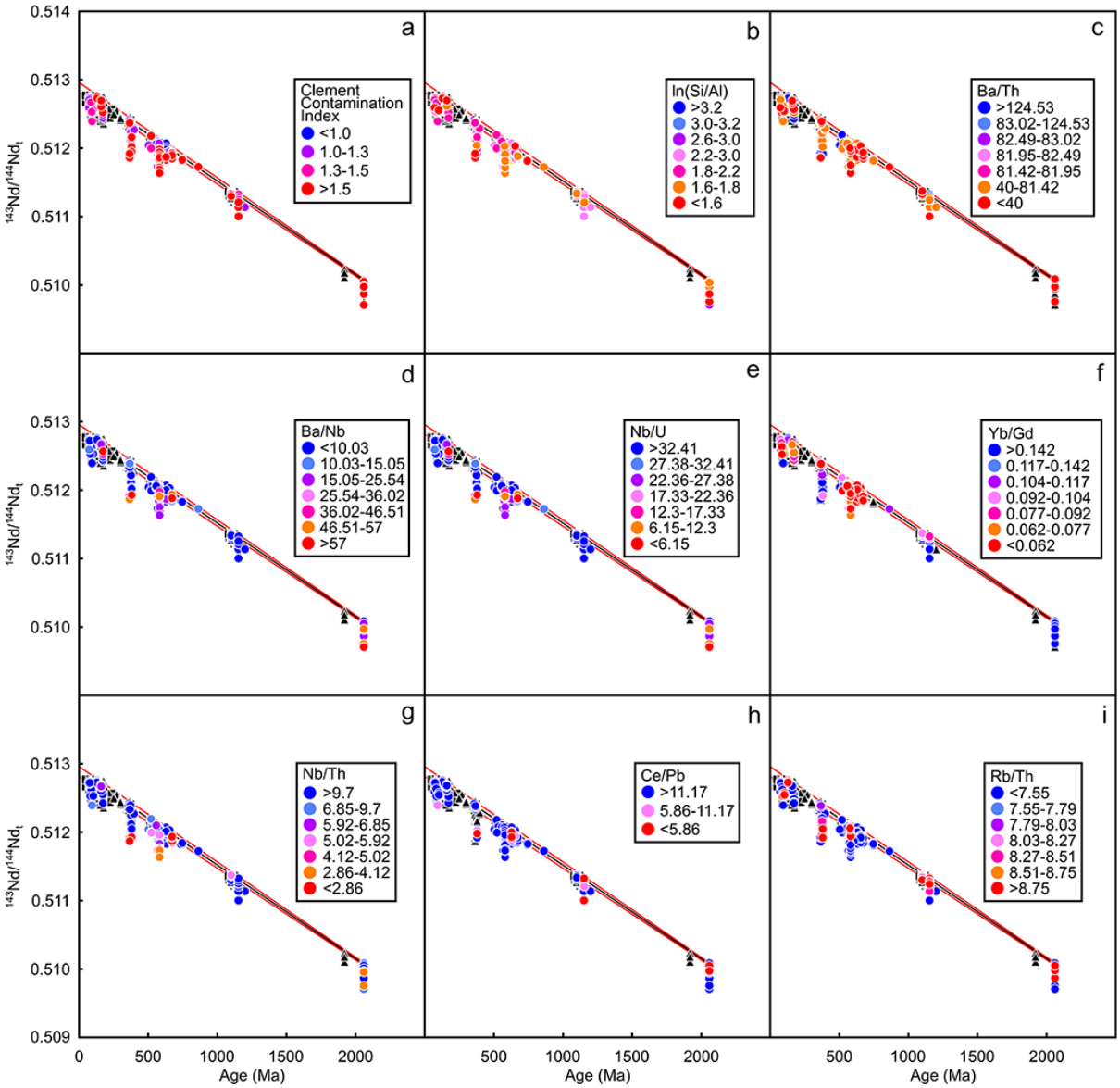

Figure S2. Major and trace element ratios in kimberlites and ultramafic lamprophyres compared to their ages and Nd isotope compositions. These major and trace element ratios are sensitive to crustal contamination, i.e. increasing Ba/Th, Ba/Nb, Yb/Gd, Rb/Th, and decreasing Si/Al, Nb/U, Nb/Th, Ce/Pb are associated with progressive crustal contamination. Geochemically enriched and transitional kimberlites are not included, while samples for which no major or trace element analyses are available are plotted using black triangles. Note that lack of any correlation between major or trace element ratios and $^{143}Nd/^{144}Nd$ values at any given time. The linear regression through the most radiogenic $^{143}Nd/^{144}Nd$ values of each province (i.e. depleted kimberlite source) is shown in black together with its 2σ uncertainty (red lines), present-day $^{143}Nd/^{144}Nd$ ratio and time-integrated $^{147}Sm/^{144}Nd$. Clement Contamination Index = $(SiO_2 + Al_2O_3 + Na_2O)/(2\times K_2O + MgO)$.

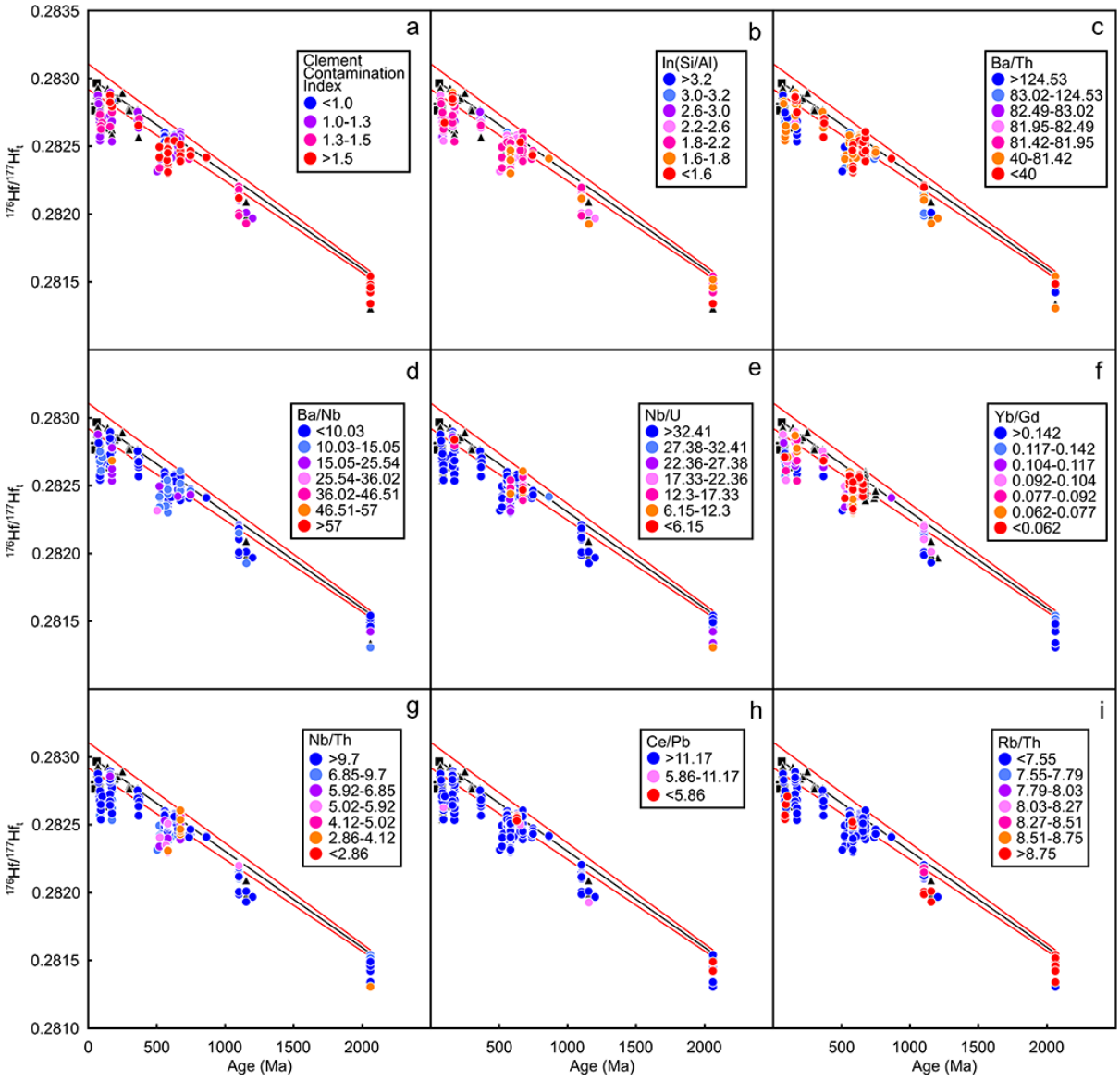

Figure S3. Major and trace element ratios in kimberlites and ultramafic lamprophyres compared to their ages and Hf isotope compositions. Note that lack of any correlation between major or trace element ratios indicative of crustal contamination and $^{176}Hf/^{177}Hf$ values at any given time. The linear regression through the most radiogenic $^{176}Hf/^{177}Hf$ values of each province (i.e. depleted kimberlite source) is shown in black together with its 2σ uncertainty (red lines), present-day $^{176}Hf/^{177}Hf$ ratio and time-integrated $^{176}Lu/^{177}Hf$. Clement Contamination Index = $(SiO_2 + Al_2O_3 + Na_2O)/(2\times K_2O + MgO)$.

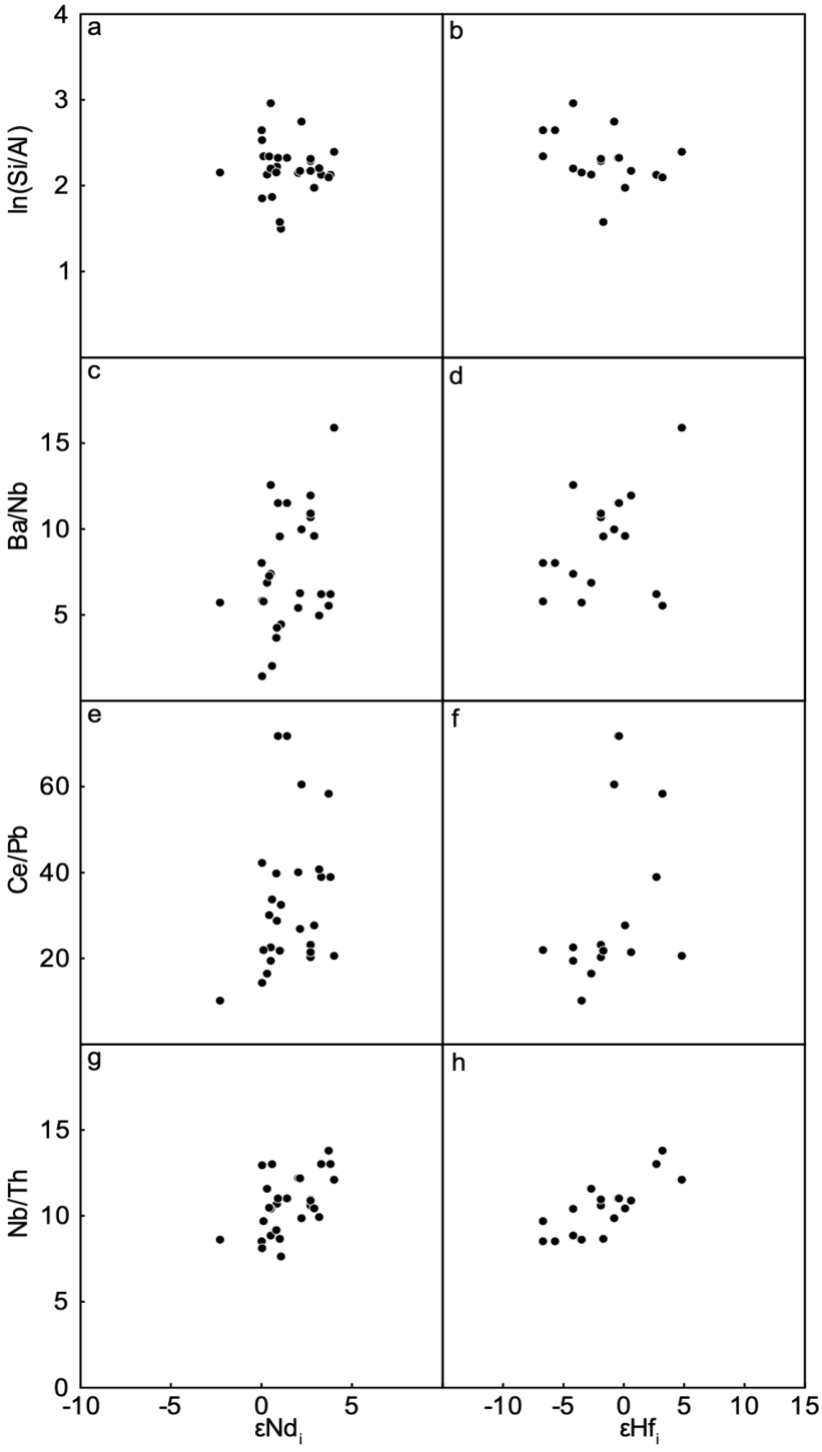

Figure S4. Representative major and trace element ratios in kimberlites from the southern African province compared to their Nd and Hf isotope compositions. Note that lack of any correlation between major or trace element ratios indicative of crustal contamination and $^{143}Nd/^{144}Nd$ or $^{176}Hf/^{177}Hf$ values.

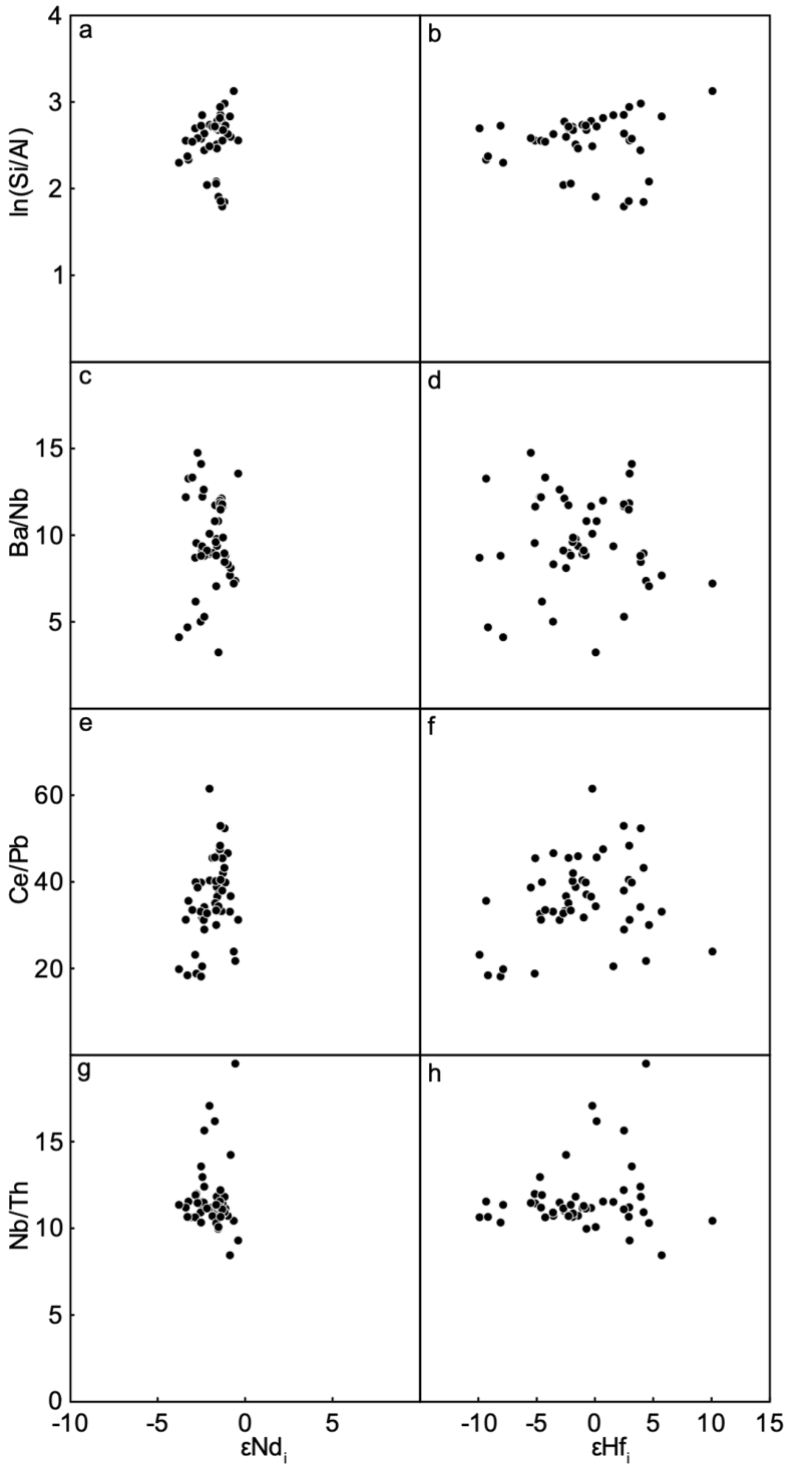

Figure S5. Representative major and trace element ratios in kimberlites from the Lac de Gras province (Canada) compared to their Nd and Hf isotope compositions. Note that lack of any correlation between major or trace element ratios indicative of crustal contamination and $^{143}Nd/^{144}Nd$ or $^{176}Hf/^{177}Hf$ values

.

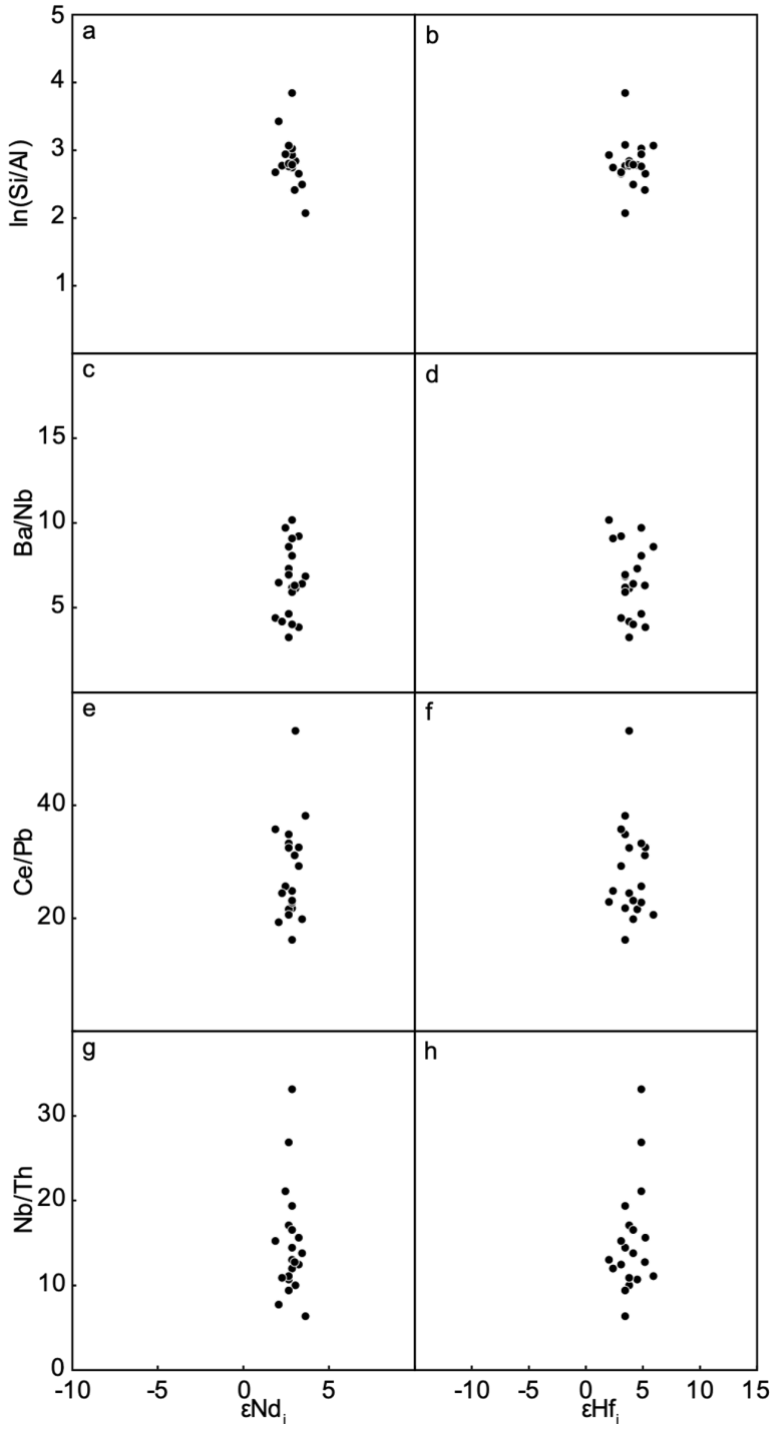

Figure S6. Representative major and trace element ratios in kimberlites from Maniitsoq (West Greenland-Labrador Neoproterozoic province) compared to their Nd and Hf isotope compositions. Note that lack of any correlation between major or trace element ratios indicative of crustal contamination and $^{143}Nd/^{144}Nd$ or $^{176}Hf/^{177}Hf$ values.

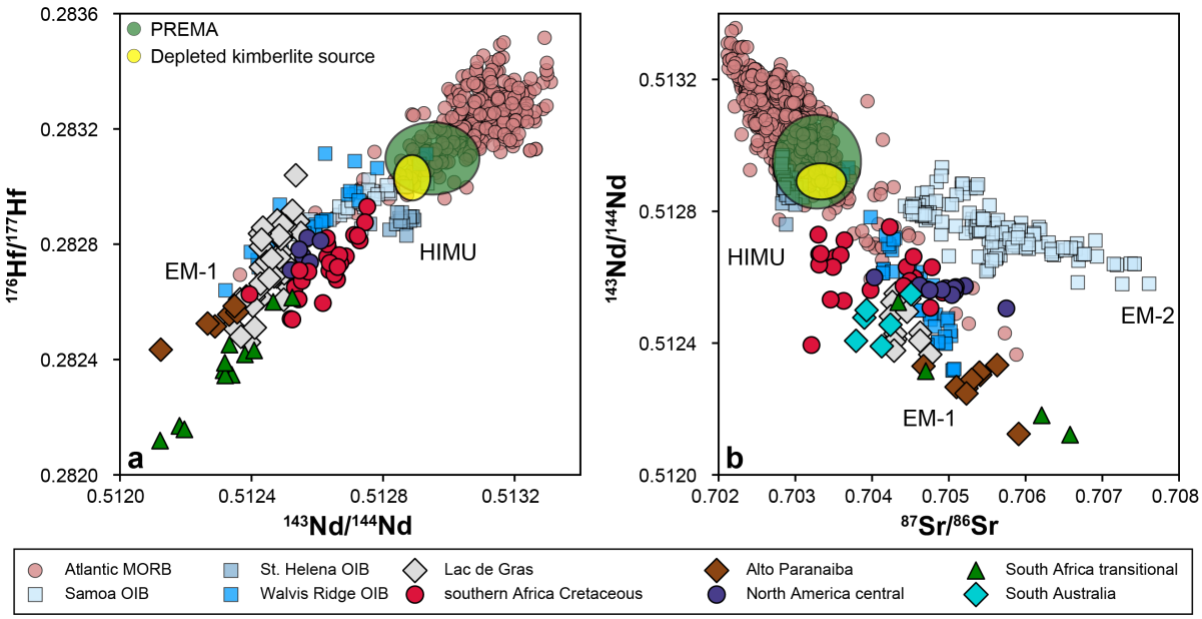

Figure S7. Sr-Nd-Hf isotope compositions of geochemically enriched kimberlites compared to southern African transitional kimberlites and ocean island basalts (OIB) endmembers. a. $^{87}Sr/^{86}Sr$ *vs* $^{143}Nd/^{144}Nd$; **b**. $^{143}Nd/^{144}Nd$ *vs* $^{176}Hf/^{177}Hf$. All the isotopic ratios of kimberlites represent initial values corrected for radiogenic ingrowth using their emplacement ages. Beyond Samoa, only Atlantic OIB have been plotted because the geochemically enriched kimberlites are preferentially located in relative proximity to the Atlantic Ocean, except for Lac de Gras in western Canada. Atlantic MORB are shown for comparison. EM: enriched mantle; HIMU: high $^{238}U/^{204}Pb$. OIB and MORB data are from the compilation of Stracke ***(11)***.

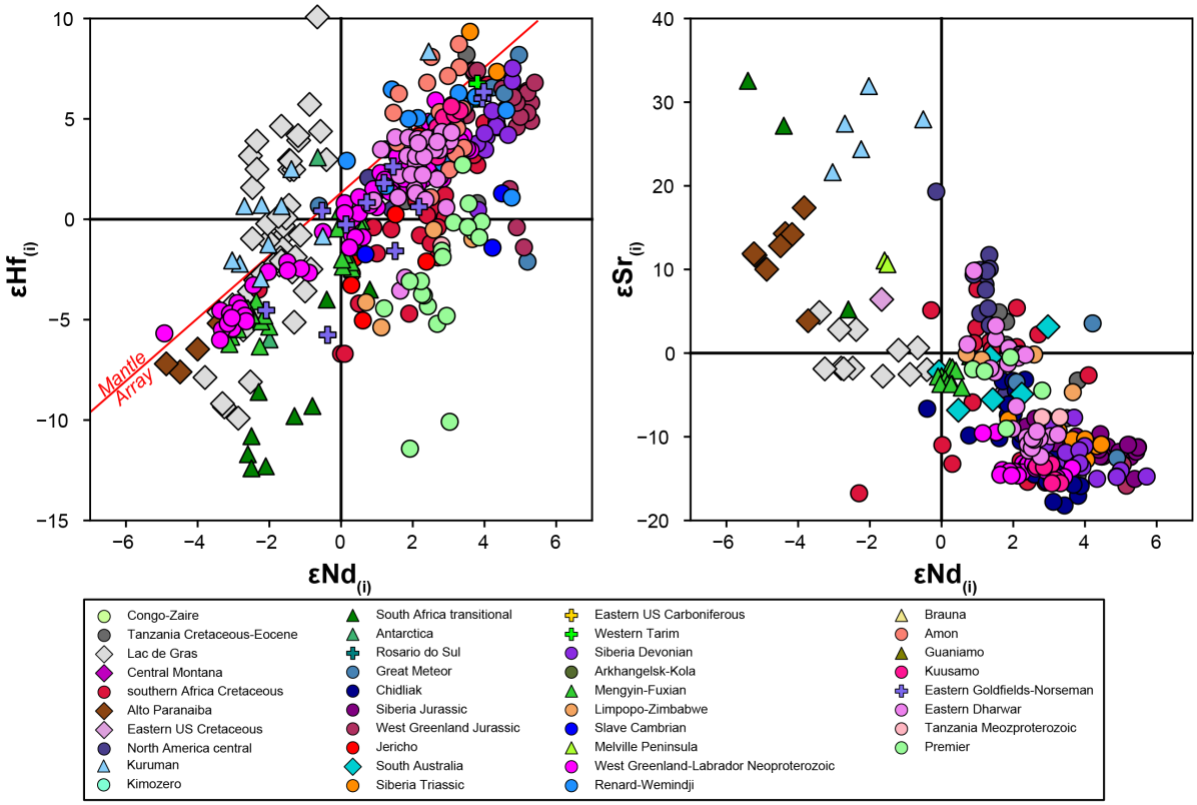

Figure S8. Sr-Nd-Hf isotope compositions of kimberlites and ultramafic lamprophyres worldwide. a. εNd *vs* εHf; b. εSr *vs* εNd. All the isotopic values have been corrected for radiogenic ingrowth using kimberlite emplacement ages. The εNd and εHf values have been calculated using the Chondritic Uniform Reservoir (CHUR) composition of Bouvier et al. (2008), while for εSr notation the following values have been employed: $^{87}Sr/^{86}Sr_{present\ day}$ = 0.7045 and $^{87}Rb/^{86}Sr$ = 0.0827. Nd-Hf mantle array from Chauvel et al. ***(79)***.

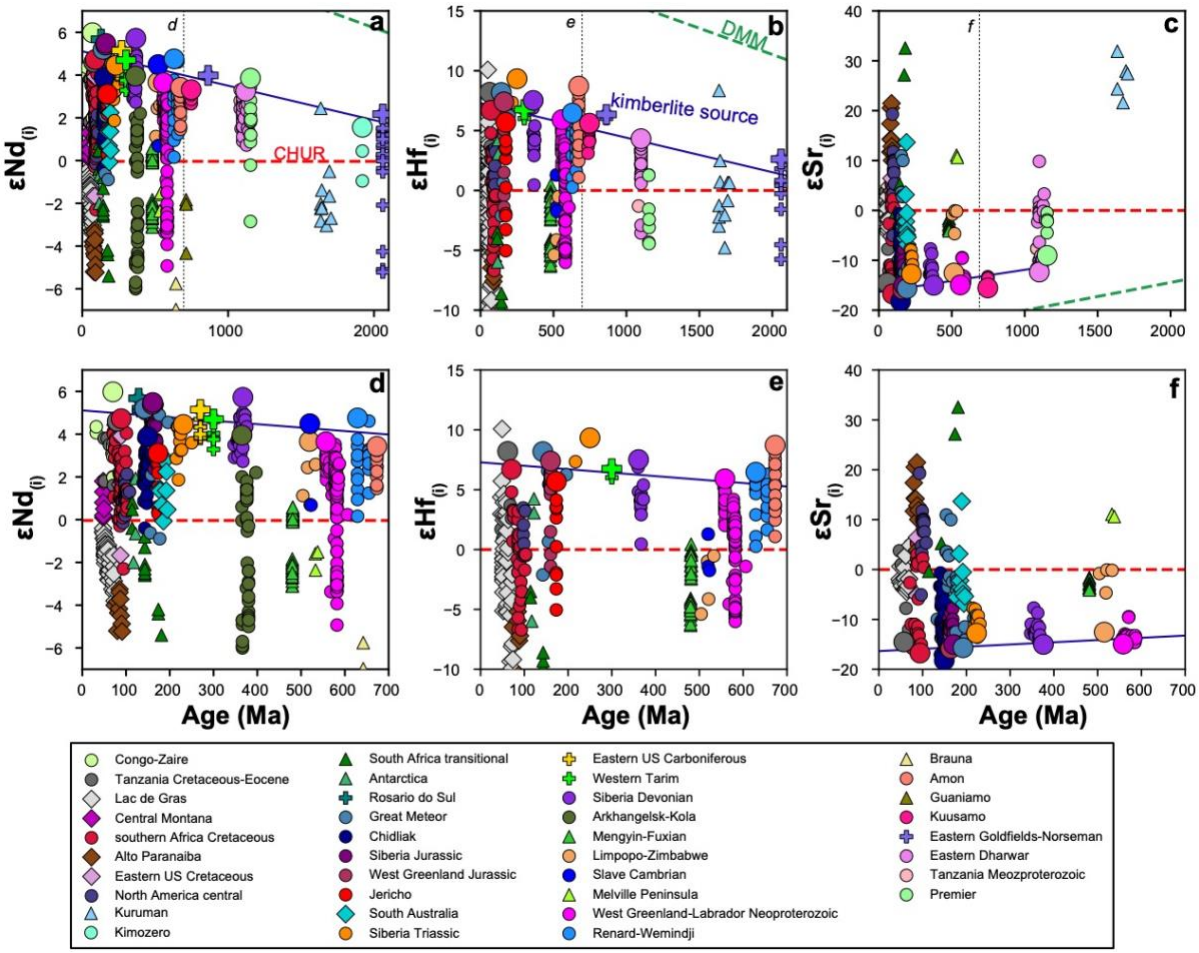

Figure S9. Nd, Hf and Sr isotope evolution of kimberlites and ultramafic lamprophyres through time. a. εNd *vs* time; **b**. εHf *vs* time; **c**. εSr *vs* time. Panels **d**, **e** and **f** show the last 700 million years of isotopic evolution for the Nd, Hf and Sr isotope systems, respectively. All the isotopic ratios represent initial values corrected for radiogenic ingrowth using the emplacement ages of kimberlites and ultramafic lamprophyres. The depleted kimberlite source evolution (dark blue line) represents a linear regression through the most radiogenic Nd and Hf and least radiogenic Sr isotopic values (i.e. larger symbols) of kimberlites (circles) and ultramafic lamprophyres (crosses) from each province. The provinces that contain geochemically enriched kimberlites (diamonds) and transitional kimberlites (triangles) are excluded from these regressions. The εNd and εHf values have been calculated using the Chondritic Uniform Reservoir (CHUR) composition of Bouvier et al. ***(41)***, while for εSr notation the following values have been employed: $^{87}Sr/^{86}Sr_{present\ day}$ = 0.7045 and $^{87}Rb/^{86}Sr$ = 0.0827. Nd-Hf mantle array from Chauvel et al. ***(79)***.

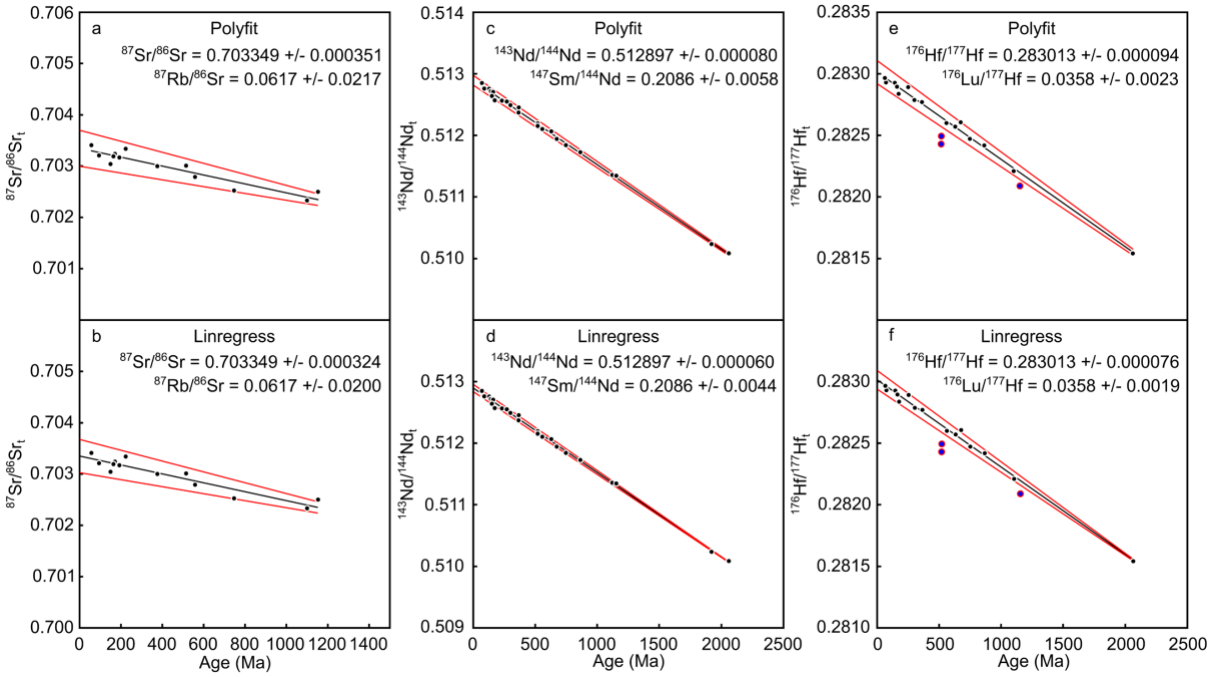

Figure S10. Sr-Nd-Hf isotope evolution of the depleted kimberlite source given by linear regressions through the least radiogenic $^{87}Sr/^{86}Sr$ and most radiogenic $^{143}Nd/^{144}Nd$ and $^{176}Hf/^{177}Hf$ ratios of each province (black lines with 2σ uncertainty envelope in red) in **a-b** $^{87}Sr/^{86}Sr$ *vs* time, **c-d** $^{143}Nd/^{144}Nd$ *vs* time, and **e-f** $^{176}Hf/^{177}Hf$ *vs* time charts. Present-day $^{87}Sr/^{86}Sr$, $^{143}Nd/^{144}Nd$ and $^{176}Hf/^{177}Hf$ ratios, and time-integrated $^{87}Rb/^{86}Sr$, $^{147}Sm/^{144}Nd$ $^{176}Lu/^{177}Hf$ ratios are also shown. Three outliers in the $^{176}Hf/^{177}Hf$ *vs* time charts are indicated with blue symbols and are not included in the regressions. The outputs of two regression methods, 'numpy.polyfit' and 'scipy.stats.linregress', based on squared errors minimization are shown for comparison and show indistinguishable results.

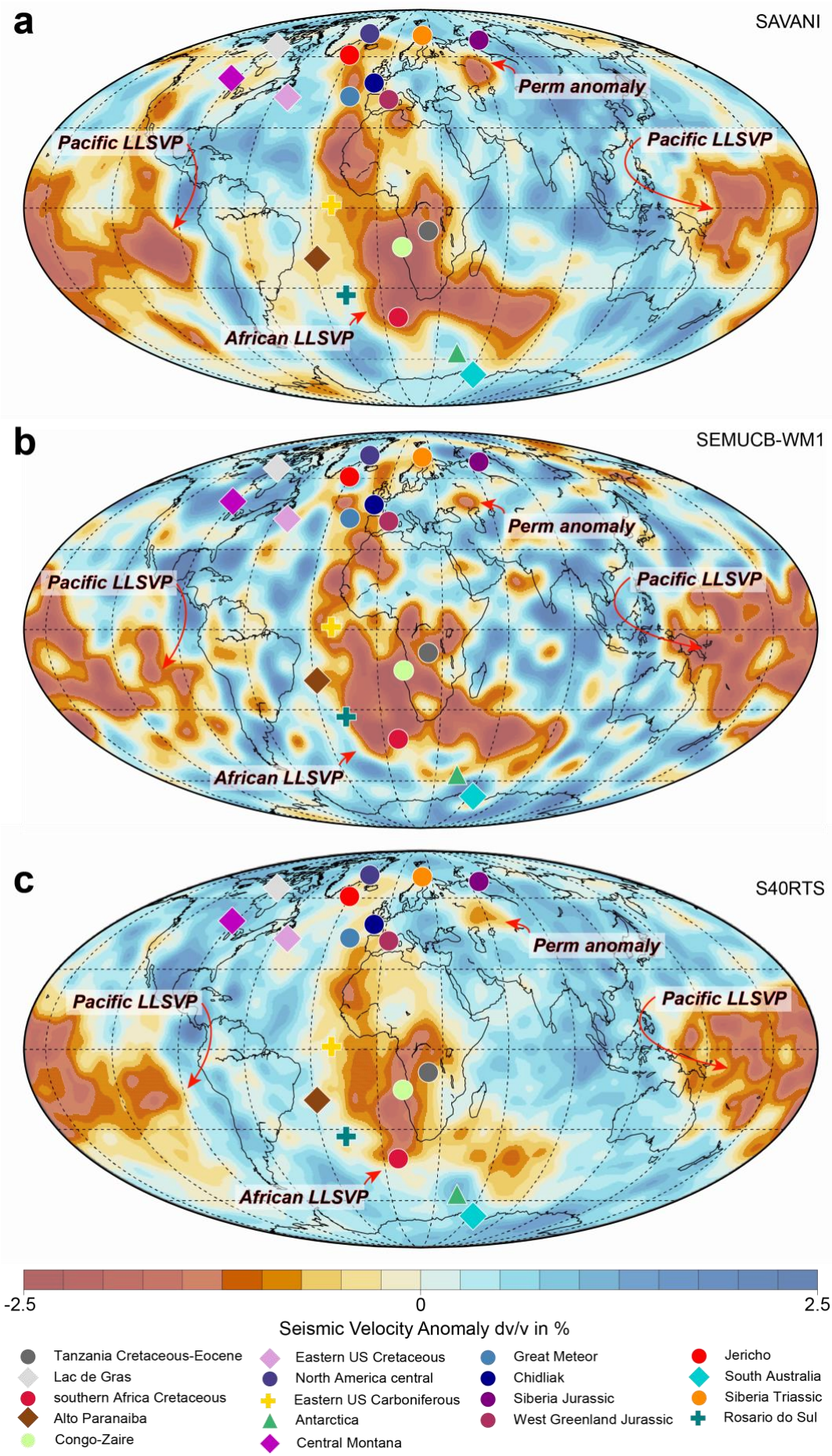
a
SAVANI
Perm anomaly
Pacific LLSVP
Pacific LLSVP
African LLSVP
b
SEMUCB-WM1
Perm anomaly
Pacific LLSVP
Pacific LLSVP
African LLSVP
c
S40RTS
Perm anomaly
Pacific LLSVP
Pacific LLSVP
African LLSVP
-2.5
0
2.5
Seismic Velocity Anomaly dv/v in %
Tanzania Cretaceous-Eocene
Lac de Gras
southern Africa Cretaceous
Alto Paranaiba
Congo-Zaire
Eastern US Cretaceous
North America central
Eastern US Carboniferous
Antarctica
Central Montana
Great Meteor
Chidliak
Siberia Jurassic
West Greenland Jurassic
Jericho
South Australia
Siberia Triassic
Rosario do Sul

Figure S11. Geographic distribution of kimberlite and ultramafic lamprophyre provinces within the last 270 million years at time of eruption, compared to the position of large low shearwave velocity provinces (LLSVPs) above the core mantle boundary. The reconstruction of kimberlite and ultramafic lamprophyre locations was undertaken using GPlates ***(58)*** paired with the continent rotation model of Torsvik et al. ***(54)***. The LLSVPs are defined based on the 1% (± 0.5%) slow contour of three different tomography models, a) Savani ***(59)***, b) S40RTS ***(145)***, and c) SEMUCB-WM1 ***(111)***, at a depth of ~2800 km – these models were prepared using the web-based tool SubMachine ***(175)***. Kimberlite provinces containing the PREMA component are shown using circles, while geochemically-enriched and transitional kimberlites with diamonds and triangles, respectively. Note the correspondence between kimberlites containing the PREMA component and the margins of LLSVPs at the time of kimberlite eruption with the exception of Siberian Jurassic kimberlites which are proximal to the Perm low-shearwave anomaly above the core-mantle boundary.

References

1. R. Montelli, G. Nolet, F. A. Dahlen, G. Masters, A catalogue of deep mantle plumes: New results from finite-frequency tomography. *Geochemistry, Geophysics, Geosystems* **7**, Q11007 (2006).
2. S. W. French, B. Romanowicz, Broad plumes rooted at the base of the Earth's mantle beneath major hotspots. *Nature* **525**, 95-99 (2015).
3. M. D. Kurz, W. J. Jenkins, S. R. Hart, Helium isotopic systematics of oceanic islands and mantle heterogeneity. *Nature* **297**, 43-47 (1982).
4. S. Mukhopadhyay, R. Parai, Noble Gases: A Record of Earth's Evolution and Mantle Dynamics. *Annual Review of Earth and Planetary Sciences* **47**, 389-419 (2019).
5. D. J. DePaolo, Crustal growth and mantle evolution: inferences from models of element transport and Nd and Sr isotopes. *Geochimica et Cosmochimica Acta* **44**, 1185-1196 (1980).
6. A. W. Hofmann, Chemical differentiation of the Earth: the relationship between mantle, continental crust, and oceanic crust. *Earth and Planetary Science Letters* **90**, 297-314 (1988).
7. C. G. Macpherson, D. R. Hilton, J. M. Sinton, R. J. Poreda, H. Craig, High 3He/4He ratios in the Manus backarc basin: Implications for mantle mixing and the origin of plumes in the western Pacific Ocean. *Geology* **26**, 1007-1010 (1998).
8. C. D. Williams, S. Mukhopadhyay, M. L. Rudolph, B. Romanowicz, Primitive Helium Is Sourced From Seismically Slow Regions in the Lowermost Mantle. *Geochemistry, Geophysics, Geosystems* **20**, 4130-4145 (2019).
9. S. R. Hart, E. H. Hauri, L. A. Oschmann, J. A. Whitehead, Mantle Plumes and Entrainment: Isotopic Evidence. *Science* **256**, 517 (1992).
10. A. Zindler, S. Hart, Chemical Geodynamics. *Annual Review of Earth and Planetary Sciences* **14**, 493-571 (1986).
11. A. Stracke, Earth's heterogeneous mantle: A product of convection-driven interaction between crust and mantle. *Chemical Geology* **330-331**, 274-299 (2012).
12. B. B. Hanan, D. W. Graham, Lead and Helium Isotope Evidence from Oceanic Basalts for a Common Deep Source of Mantle Plumes. *Science* **272**, 991-995 (1996).
13. A. Stracke, A. W. Hofmann, S. R. Hart, FOZO, HIMU, and the rest of the mantle zoo. *Geochemistry, Geophysics, Geosystems* **6**, Q05007 (2005).
14. M. Stein, A. W. Hofmann, Mantle plumes and episodic crustal growth. *Nature* **372**, 63-68 (1994).
15. G. Wörner, A. Zindler, H. Staudigel, H. U. Schmincke, Sr, Nd, and Pb isotope geochemistry of Tertiary and Quaternary alkaline volcanics from West Germany. *Earth and Planetary Science Letters* **79**, 107-119 (1986).
16. C. Class, S. L. Goldstein, Evolution of helium isotopes in the Earth's mantle. *Nature* **436**, 1107-1112 (2005).
17. H. Sumino, I. Kaneoka, K. Matsufuji, A. V. Sobolev, Deep mantle origin of kimberlite magmas revealed by neon isotopes. *Geophysical Research Letters* **33**, L16318 (2006).
18. Y. Tachibana, I. Kaneoka, A. Gaffney, B. Upton, Ocean-island basalt-like source of kimberlite magmas from West Greenland revealed by high 3He/4He ratios. *Geology* **34**, 273-276 (2006).
19. J. Woodhead *et al.*, Kimberlites reveal 2.5-billion-year evolution of a deep, isolated mantle reservoir. *Nature* **573**, 578-581 (2019).
20. T. H. Torsvik, K. Burke, B. Steinberger, S. J. Webb, L. D. Ashwal, Diamonds sampled by plumes from the core-mantle boundary. *Nature* **466**, 352-355 (2010).

21. L. M. Heaman, B. A. Kjarsgaard, Timing of eastern North American kimberlite magmatism: continental extension of the Great Meteor hotspot track? *Earth and Planetary Science Letters* **178**, 253-268 (2000).
22. L. M. Heaman, D. Phillips, G. Pearson, Dating Kimberlites: Methods and Emplacement Patterns Through Time. *Elements* **15**, 399-404 (2019).
23. A. Giuliani *et al.*, Kimberlite genesis from a common carbonate-rich primary melt modified by lithospheric mantle assimilation. *Science Advances* **6**, eaaz0424 (2020).
24. D. G. Pearson, J. Woodhead, P. E. Janney, Kimberlites as Geochemical Probes of Earth's Mantle. *Elements* **15**, 387-392 (2019).
25. S. Tappe *et al.*, Between carbonatite and lamproite—Diamondiferous Torngat ultramafic lamprophyres formed by carbonate-fluxed melting of cratonic MARID-type metasomes. *Geochimica et Cosmochimica Acta* **72**, 3258-3286 (2008).
26. S. Tappe, G. D. Pearson, B. A. Kjarsgaard, G. Nowell, D. Dowall, Mantle transition zone input to kimberlite magmatism near a subduction zone: Origin of anomalous Nd–Hf isotope systematics at Lac de Gras, Canada. *Earth and Planetary Science Letters* **371–372**, 235-251 (2013).
27. R. H. Mitchell, A. Giuliani, H. O'Brien, What is a Kimberlite? Petrology and Mineralogy of Hypabyssal Kimberlites. *Elements* **15**, 381-386 (2019).
28. M. Becker, A. P. le Roex, Geochemistry of South African On- and Off-craton, Group I and Group II Kimberlites: Petrogenesis and Source Region Evolution. *Journal of Petrology* **47**, 673-703 (2006).
29. B. A. Kjarsgaard, D. G. Pearson, S. Tappe, G. M. Nowell, D. P. Dowall, Geochemistry of hypabyssal kimberlites from Lac de Gras, Canada: Comparisons to a global database and applications to the parent magma problem. *Lithos* **112S**, 236-248 (2009).
30. F.-Y. Wu *et al.*, In situ U-Pb age determination and Sr-Nd isotopic analysis of perovskite from the Premier (Cullinan) kimberlite, South Africa. *Chemical Geology* **353**, 83-95 (2013).
31. A. Araujo, R. W. Carlson, J. C. Gaspar, L. A. Bizzi, Petrology of kamafugites and kimberlites from the Alto Paranaíba Alkaline Province, Minas Gerais, Brazil. *Contributions to Mineralogy and Petrology* **142**, 163-177 (2001).
32. G. M. Nowell *et al.*, Hf Isotope Systematics of Kimberlites and their Megacrysts: New Constraints on their Source Regions. *Journal of Petrology* **45**, 1583-1612 (2004).
33. J. G. Konter *et al.*, One hundred million years of mantle geochemical history suggest the retiring of mantle plumes is premature. *Earth and Planetary Science Letters* **275**, 285-295 (2008).
34. P. G. Eriksson *et al.*, Secular changes in sedimentation systems and sequence stratigraphy. *Gondwana Research* **24**, 468-489 (2013).
35. A. Ridgwell, R. E. Zeebe, The role of the global carbonate cycle in the regulation and evolution of the Earth system. *Earth and Planetary Science Letters* **234**, 299-315 (2005).
36. W. J. McMahon, N. S. Davies, Evolution of alluvial mudrock forced by early land plants. *Science* **359**, 1022-1024 (2018).
37. R. M. Holder, D. R. Viete, M. Brown, T. E. Johnson, Metamorphism and the evolution of plate tectonics. *Nature* **572**, 378-381 (2019).
38. C. Herzberg, K. Condie, J. Korenaga, Thermal history of the Earth and its petrological expression. *Earth and Planetary Science Letters* **292**, 79-88 (2010).

39. S. Aulbach *et al.*, Evidence for a dominantly reducing Archaean ambient mantle from two redox proxies, and low oxygen fugacity of deeply subducted oceanic crust. *Scientific Reports* **9**, 20190 (2019).
40. C. B. Keller, B. Schoene, Statistical geochemistry reveals disruption in secular lithospheric evolution about 2.5 Gyr ago. *Nature* **485**, 490-493 (2012).
41. A. Bouvier, J. D. Vervoort, P. J. Patchett, The Lu-Hf and Sm-Nd isotopic composition of CHUR: Constraints from unequilibrated chondrites and implications for the bulk composition of terrestrial planets. *Earth and Planetary Science Letters* **273**, 48-57 (2008).
42. G. Caro, B. Bourdon, Non-chondritic Sm/Nd ratio in the terrestrial planets: Consequences for the geochemical evolution of the mantle–crust system. *Geochimica et Cosmochimica Acta* **74**, 3333-3349 (2010).
43. M. Boyet, R. W. Carlson, 142Nd Evidence for Early (>4.53 Ga) Global Differentiation of the Silicate Earth. *Science* **309**, 576-581 (2005).
44. A. Bouvier, M. Boyet, Primitive Solar System materials and Earth share a common initial 142Nd abundance. *Nature* **537**, 399-402 (2016).
45. C. Burkhardt *et al.*, A nucleosynthetic origin for the Earth's anomalous 142Nd composition. *Nature* **537**, 394-398 (2016).
46. A. Gannoun, M. Boyet, H. Rizo, A. El Goresy, 146Sm–142Nd systematics measured in enstatite chondrites reveals a heterogeneous distribution of 142Nd in the solar nebula. *Proceedings of the National Academy of Sciences* **108**, 7693-7697 (2011).
47. G. A. M. de Leeuw, R. M. Ellam, F. M. Stuart, R. W. Carlson, 142Nd/144Nd inferences on the nature and origin of the source of high 3He/4He magmas. *Earth and Planetary Science Letters* **472**, 62-68 (2017).
48. L. N. Willhite *et al.*, Hot and Heterogenous High-3He/4He Components: New Constraints From Proto-Iceland Plume Lavas From Baffin Island. *Geochemistry, Geophysics, Geosystems* **20**, 5939-5967 (2020).
49. M. Maurice, N. Tosi, S. Schwinger, D. Breuer, T. Kleine, A long-lived magma ocean on a young Moon. *Science Advances* **6**, eaba8949 (2020).
50. R. W. Carlson, M. Garçon, J. O'Neil, J. Reimink, H. Rizo, The nature of Earth's first crust. *Chemical Geology* **530**, 119321 (2019).
51. M. G. Jackson *et al.*, Evidence for the survival of the oldest terrestrial mantle reservoir. *Nature* **466**, 853-856 (2010).
52. K. Burke, B. Steinberger, T. H. Torsvik, M. A. Smethurst, Plume Generation Zones at the margins of Large Low Shear Velocity Provinces on the core–mantle boundary. *Earth and Planetary Science Letters* **265**, 49-60 (2008).
53. C. P. Conrad, B. Steinberger, T. H. Torsvik, Stability of active mantle upwelling revealed by net characteristics of plate tectonics. *Nature* **498**, 479-482 (2013).
54. T. H. Torsvik *et al.*, Deep mantle structure as a reference frame for movements in and on the Earth. *Proceedings of the National Academy of Sciences* **111**, 8735 (2014).
55. K. D. Collerson, Q. Williams, A. E. Ewart, D. T. Murphy, Origin of HIMU and EM-1 domains sampled by ocean island basalts, kimberlites and carbonatites: The role of CO2-fluxed lower mantle melting in thermochemical upwellings. *Physics of the Earth and Planetary Interiors* **181**, 112-131 (2010).
56. M. G. Jackson, T. W. Becker, J. G. Konter, Geochemistry and Distribution of Recycled Domains in the Mantle Inferred From Nd and Pb Isotopes in Oceanic Hot Spots: Implications for Storage in the Large Low Shear Wave Velocity Provinces. *Geochemistry, Geophysics, Geosystems* **19**, 3496-3519 (2018).
57. S. Labrosse, J. W. Hernlund, N. Coltice, A crystallizing dense magma ocean at the base of the Earth's mantle. *Nature* **450**, 866-869 (2007).

58. R. D. Müller *et al.*, GPlates: Building a Virtual Earth Through Deep Time. *Geochemistry, Geophysics, Geosystems* **19**, 2243-2261 (2018).
59. L. Auer, L. Boschi, T. W. Becker, T. Nissen-Meyer, D. Giardini, Savani: A variable resolution whole-mantle model of anisotropic shear velocity variations based on multiple data sets. *Journal of Geophysical Research: Solid Earth* **119**, 3006-3034 (2014).
60. S. Cottaar, V. Lekic, Morphology of seismically slow lower-mantle structures. *Geophysical Journal International* **207**, 1122-1136 (2016).
61. H. Dalton *et al.*, Petrogenesis of a hybrid cluster of evolved kimberlites and ultramafic lamprophyres in the Kuusamo area, Finland. *Journal of Petrology*, (2020).
62. R. H. Mitchell, B. H. Scott Smith, L. M. Larsen, in *Proceedings of the 7th International KImberlite Conference,* J. J. Gurney, J. L. Gurney, M. D. Pascoe, S. H. Richardson, Eds. (Red Roof Design, Cape Town, 1999), vol. 2, pp. 574-583.
63. C. B. Smith, S. E. Haggerty, B. Chatterjee, A. Beard, R. Townend, Kimberlite, lamproite, ultramafic lamprophyre, and carbonatite relationships on the Dharwar Craton, India; an example from the Khaderpet pipe, a diamondiferous ultramafic with associated carbonatite intrusion. *Lithos* **182-183**, 102-113 (2013).
64. S. Tappe *et al.*, Genesis of Ultramafic Lamprophyres and Carbonatites at Aillik Bay, Labrador: a Consequence of Incipient Lithospheric Thinning beneath the North Atlantic Craton. *Journal of Petrology* **47**, 1261-1315 (2006).
65. R. H. Mitchell, *Kimberlites, Orangeites and Related Rocks*. (Plenum Press, New York, 1995), pp. 410.
66. B. H. Scott Smith *et al.*, *A Glossary of kimberlite and related rocks*. (Scott-Smith Petrology Inc., North Vancouver, Canada, 2018), pp. Part 1 – 144 pp; Part 142 – 159 pp; Part 143 – 156 pp.
67. A. Giuliani *et al.*, Did diamond-bearing orangeites originate from MARID-veined peridotites in the lithospheric mantle? *Nature Communications* **6**, 6837 (2015).
68. R. H. Mitchell, *Kimberlites: Mineralogy, Geochemistry and Petrology.*, (Plenum Publishing Company, New York, 1986), pp. 442.
69. S. Tappe, S. F. Foley, G. A. Jenner, B. A. Kjarsgaard, Integrating Ultramafic Lamprophyres into the IUGS Classification of Igneous Rocks: Rationale and Implications. *Journal of Petrology* **46**, 1893-1900 (2005).
70. N. V. Chalapathi Rao, R. K. Srivastava, Petrology and geochemistry of diamondiferous Mesoproterozoic kimberlites from Wajrakarur kimberlite field, Eastern Dharwar craton, southern India: genesis and constraints on mantle source regions. *Contributions to Mineralogy and Petrology* **157**, 245-265 (2009).
71. G. Kaur, M. M. Korakoppa, Fareeduddin, K. L. Pruseth, in *Proceedings of 10th International Kimberlite Conference,* D. G. Pearson *et al.*, Eds. (Springer India, New Delhi, 2013), pp. 183-194.
72. C. Paton, J. M. Hergt, J. D. Woodhead, D. Phillips, S. R. Shee, Identifying the asthenospheric component of kimberlite magmas from the Dharwar Craton, India. *Lithos* **112S**, 296-310 (2009).
73. A. M. Shaikh *et al.*, The P3 kimberlite and P4 lamproite, Wajrakarur kimberlite field, India: mineralogy, and major and minor element compositions of olivines as records of their phenocrystic vs xenocrystic origin. *Mineralogy and Petrology* **112**, 609-624 (2018).
74. J. Woodhead, J. Hergt, D. Phillips, C. Paton, African kimberlites revisited: In situ Sr-isotope analysis of groundmass perovskite. *Lithos* **112S**, 311-317 (2009).
75. W. F. McDonough, S. S. Sun, The composition of the Earth. *Chemical Geology* **120**, 223-253 (1995).

76. R. L. Rudnick, S. Gao, in *Treatise on Geochemistry (Second Edition),* H. D. Turekian, K. K. Holland, Eds. (Elsevier, Oxford, 2014), vol. Vol. 4. The Crust, pp. 1-51.
77. G. P. Bulanova *et al.*, Mineral inclusions in sublithospheric diamonds from Collier 4 kimberlite pipe, Juina, Brazil: subducted protoliths, carbonated melts and primary kimberlite magmatism. *Contributions to Mineralogy and Petrology* **160**, 489-510 (2010).
78. B. Harte, S. Richardson, Mineral inclusions in diamonds track the evolution of a Mesozoic subducted slab beneath West Gondwanaland. *Gondwana Research* **21**, 236-245 (2012).
79. C. Chauvel, E. Lewin, M. Carpentier, N. T. Arndt, J.-C. Marini, Role of recycled oceanic basalt and sediment in generating the Hf-Nd mantle array. *Nature Geosci* **1**, 64-67 (2008).
80. A. Stracke, M. Bizimis, V. J. M. Salters, Recycling oceanic crust: Quantitative constraints. *Geochemistry, Geophysics, Geosystems* **4**, 8003 (2003).
81. A. Abersteiner, A. Giuliani, V. S. Kamenetsky, D. Phillips, Petrographic and melt-inclusion constraints on the petrogenesis of a magmaclast from the Venetia kimberlite cluster, South Africa. *Chemical Geology* **455**, 331-341 (2017).
82. A. M. Agashev *et al.*, Geochemistry and origin of the Mirny field kimberlites, Siberia. *Mineralogy and Petrology* **112**, 597-608 (2018).
83. C. Alibert, F. Albarede, Relationships between mineralogical, chemical, and isotopic properties of some North American kimberlites. *Journal of Geophysical Research: Solid Earth* **93**, 7643-7671 (1988).
84. H. L. Allsopp, D. R. Barrett, Rb-Sr age determinations on South African kimberlite pipes. *Physics and Chemistry of the Earth* **9**, 605-617 (1975).
85. H. L. Allsopp, J. D. Kramers, Rb-Sr and U-Pb determinations on southern African kimberlite pipes. *2nd International Kimberlite Conference, Extended Abstracts*, (1977).
86. H. L. Allsopp, C. B. Smith, A. G. Seggie, E. M. W. Skinner, E. A. Colgan, The emplacement age and geochemical character of the Venetia kimberlite bodies, Limpopo Belt, northern Transvaal. *South African Journal of Geology* **98**, 239-244 (1995).
87. J. P. Armstrong, M. Wilson, R. L. Barnett, T. Nowicki, B. A. Kjarsgaard, Mineralogy of primary carbonate-bearing hypabyssal kimberlite, Lac de Gras, Slave Province, Northwest Territories, Canada. *Lithos* **76**, 415-433 (2004).
88. J. M. Batumike *et al.*, LAM-ICPMS U-Pb dating of kimberlitic perovskite: Eocene-Oligocene kimberlites from the Kundelungu Plateau, D.R. Congo. *Earth and Planetary Science Letters* **267**, 609-619 (2008).
89. A. D. Beard, H. Downes, E. Hegner, S. M. Sablukov, Geochemistry and mineralogy of kimberlites from the Arkhangelsk Region, NW Russia: evidence for transitional kimberlite magma types. *Lithos* **51**, 47-73 (2000).
90. A. D. Beard *et al.*, Mineralogy and geochemistry of Devonian ultramafic minor intrusions of the southern Kola Peninsula, Russia: implications for the petrogenesis of kimberlites and melilitites. *Contributions to Mineralogy and Petrology* **130**, 288-303 (1998).
91. M. Bizzarro, A. Simonetti, R. K. Stevenson, J. David, Hf isotope evidence for a hidden mantle reservoir. *Geology* **30**, 771-774 (2002).
92. R. W. Carlson, G. Czamanske, V. Fedorenko, I. Ilupin, A comparison of Siberian meimechites and kimberlites: Implications for the source of high-Mg alkalic magmas and flood basalts. *Geochem. Geophys. Geosyst.* **7**, Q11014 (2006).

93. G. Caro, M. G. Kopylova, R. A. Creaser, The hypabyssal 5034 kimberlite of the Gahcho Kue cluster, southeastern Slave Craton, Northwest Territories, Canada: A granite-contaminated Group I kimberlite. *The Canadian Mineralogist* **42**, 183-207 (2004).
94. N. V. Chalapathi Rao, F.-Y. Wu, R. H. Mitchell, Q.-L. Li, B. Lehmann, Mesoproterozoic U–Pb ages, trace element and Sr–Nd isotopic composition of perovskite from kimberlites of the Eastern Dharwar craton, southern India: Distinct mantle sources and a widespread 1.1 Ga tectonomagmatic event. *Chemical Geology* **353**, 48-64 (2013).
95. Z. Cheng, Z. Zhang, M. Santosh, T. Hou, D. Zhang, Carbonate- and silicate-rich globules in the kimberlitic rocks of northwestern Tarim large igneous province, NW China: Evidence for carbonated mantle source. *Journal of Asian Earth Sciences* **95**, 114-135 (2014).
96. R. Chesler, The University of Melbourne, (2012).
97. E. Choi *et al.*, Subduction-related petrogenesis of Late Archean calc-alkaline lamprophyres in the Yilgarn Craton (Western Australia). *Precambrian Research* **338**, 105550 (2020).
98. R. V. Conceição, L. C. Carniel, T. Jalowitzki, F. Gervasoni, D. G. Cedeño, Geochemistry and geodynamic implications on the source of Paraná-Etendeka Large Igneous Province evidenced by the 128 Ma Rosário-6 kimberlite, southern Brazil. *Lithos* **328-329**, 130-145 (2019).
99. R. A. Creaser, H. Grütter, J. Carlson, B. Crawford, Macrocrystal phlogopite Rb–Sr dates for the Ekati property kimberlites, Slave Province, Canada: evidence for multiple intrusive episodes in the Paleocene and Eocene. *Lithos* **76**, 399-414 (2004).
100. H. Dalton *et al.*, A comparison of geochronological methods commonly applied to kimberlites and related rocks: Three case studies from Finland. *Chemical Geology* **558**, 119899 (2020).
101. G. R. Davies, A. J. Spriggs, P. H. Nixon, A Non-cognate Origin for the Gibeon Kimberlite Megacryst Suite, Namibia: Implications for the Origin of Namibian Kimberlites. *Journal of Petrology* **42**, 159-172 (2001).
102. G. L. Davis, The ages and uranium content of zircons from kimberlites and associated rocks. *Carnegie Institute Washington Yearbook* **76**, 631-635 (1977).
103. J. P. Donatti-Filho, S. Tappe, E. P. Oliveira, L. M. Heaman, Age and origin of the Neoproterozoic Brauna kimberlites: Melt generation within the metasomatized base of the São Francisco craton, Brazil. *Chemical Geology* **353**, 19-35 (2013).
104. A. Dongre, S. Tappe, Kimberlite and carbonatite dykes within the Premier diatreme root (Cullinan Diamond Mine, South Africa): New insights to mineralogical-genetic classifications and magma CO2 degassing. *Lithos* **338-339**, 155-173 (2019).
105. C. Donnelly, W. Griffin, S. O'Reilly, N. Pearson, S. Shee, The Kimberlites and related rocks of the Kuruman Kimberlite Province, Kaapvaal Craton, South Africa. *Contributions to Mineralogy and Petrology* **161**, 351-371 (2011).
106. C. L. Donnelly *et al.*, In situ U-Pb Dating and Sr-Nd Isotopic Analysis of Perovskite: Constraints on the Age and Petrogenesis of the Kuruman Kimberlite Province, Kaapvaal Craton, South Africa. *Journal of Petrology* **53**, 2497-2522 (2012).
107. D. P. Dowall, Durham University, (2004).
108. H. Downes, E. Balaganskaya, A. Beard, R. Liferovich, D. Demaiffe, Petrogenetic processes in the ultramafic, alkaline and carbonatitic magmatism in the Kola Alkaline Province: A review. *Lithos* **85**, 48-75 (2005).
109. M. R. Felgate, The University of Melbourne, (2014).

110. M. L. Fiorentini *et al.*, Bushveld super plume drove Proterozoic magmatism and metallogenesis in Australia. *Scientific Reports*, (in press).
111. S. W. French, B. A. Romanowicz, Whole-mantle radially anisotropic shear velocity structure from spectral-element waveform tomography. *Geophysical Journal International* **199**, 1303-1327 (2014).
112. A. M. Gaffney *et al.*, Constraints on source-forming processes of West Greenland kimberlites inferred from Hf-Nd isotope systematics. *Geochimica et Cosmochimica Acta* **71**, 2820-2836 (2007).
113. T. M. Gernon, M. Field, R. S. J. Sparks, Geology of the Snap Lake kimberlite intrusion, Northwest Territories, Canada: field observations and their interpretation. *Journal of the Geological Society* **169**, 1-16 (2012).
114. A. Giuliani, D. G. Pearson, Kimberlites: From Deep Earth to Diamond Mines. *Elements* **15**, 377-380 (2019).
115. S. Graham, D. Lambert, S. Shee, The petrogenesis of carbonatite, melnoite and kimberlite from the Eastern Goldfields Province, Yilgarn Craton. *Lithos* **76**, 519-533 (2004).
116. W. L. Griffin *et al.*, Emplacement ages and sources of kimberlites and related rocks in southern Africa: U–Pb ages and Sr–Nd isotopes of groundmass perovskite. *Contributions to Mineralogy and Petrology* **168**, 1032-1045 (2014).
117. V. Guarino *et al.*, U–Pb ages, Sr–Nd- isotope geochemistry, and petrogenesis of kimberlites, kamafugites and phlogopite-picrites of the Alto Paranaíba Igneous Province, Brazil. *Chemical Geology* **353**, 65-82 (2013).
118. L. M. Heaman, The nature of the subcontinental mantle from Sr-Nd-Pb isotopic studies on kimberlitic perovskite. *Earth and Planetary Science Letters* **92**, 323-334 (1989).
119. L. M. Heaman, R. A. Creaser, H. O. Cookenboo, T. O. M. Chacko, Multi-Stage Modification of the Northern Slave Mantle Lithosphere: Evidence from Zircon- and Diamond-Bearing Eclogite Xenoliths Entrained in Jericho Kimberlite, Canada. *Journal of Petrology* **47**, 821-858 (2006).
120. L. M. Heaman, B. A. Kjarsgaard, R. A. Creaser, The timing of kimberlite magmatism in North America: implications for global kimberlite genesis and diamond exploration. *Lithos* **71**, 153-184 (2003).
121. L. M. Heaman, B. A. Kjarsgaard, R. A. Creaser, The temporal evolution of North American kimberlites. *Lithos* **76**, 377-397 (2004).
122. L. M. Heaman, J. Pell, H. S. Grütter, R. A. Creaser, U–Pb geochronology and Sr/Nd isotope compositions of groundmass perovskite from the newly discovered Jurassic Chidliak kimberlite field, Baffin Island, Canada. *Earth and Planetary Science Letters* **415**, 183-199 (2015).
123. B. C. Hearn Jr, in *Kimberlites and Related Rocks. 4th International Kimberlite Conference,* J. Ross *et al.*, Eds. (Geological Society of Australia, Perth, 1989), vol. 1, pp. 109-119.
124. E. Hegner, J. C. Roddick, S. M. Fortier, L. Hulbert, Nd, Sr, Pb, Ar and O isotopic systematics of Sturgeon Lake kimberlite, Saskatchewan, Canada: constraints on emplacement age, alteration and source composition. *Contributions to Mineralogy and Petrology* **120**, 212-222 (1995).
125. R. H. Hunter, R. D. Kissling, L. A. Taylor, Mid to late-stage kimberlitic melt evolution: phlogopites and oxides from the Fayette County kimberlite, Pennsylvania. *American Mineralogist* **69**, 30-40 (1984).

126. C. Y. Jiang, P. B. Zhang, D. R. Lu, K. Y. Bai, Petrogenesis and magma source of the ultramafic rocks at Wajilitag region, western Tarim plate in Xinjiang. *Acta Petrologica Sinica* **20**, 1433-1444 (2004).
127. V. S. Kamenetsky *et al.*, Chlorine from the mantle: Magmatic halides in the Udachnaya-East kimberlite, Siberia. *Earth and Planetary Science Letters* **285**, 96-104 (2009).
128. F. V. Kaminsky, S. M. Sablukov, L. I. Sablukova, D. M. D. Channer, Neoproterozoic 'anomalous' kimberlites of Guaniamo, Venezuela: Mica kimberlites of 'isotopic transitional' type. *Lithos* **76**, 565-590 (2004).
129. P. D. Kinny, W. Compston, J. W. Bristow, I. S. Williams, in *Kimberlites and Related Rocks. 4th International Kimberlite Conference,* J. Ross *et al.*, Eds. (Geological Society of Australia, Perth, 1989), vol. 2, pp. 833-842.
130. P. D. Kinny, B. J. Griffin, L. M. Heaman, F. F. Brakhfogel, Z. V. Spetius, SHRIMP U-Pb ages of perovskite from Yakutian kimberlites. *Russian Geology and Geophysics* **38**, 97-105 (1997).
131. B. A. Kjarsgaard *et al.*, Geology of the Orion South kimberlite, Fort à la Corne, Canada. *Lithos* **112**, 600-617 (2009).
132. B. A. Kjarsgaard, L. M. Heaman, C. Sarkar, D. G. Pearson, The North America mid-Cretaceous kimberlite corridor: Wet, edge-driven decompression melting of an OIB-type deep mantle source. *Geochemistry, Geophysics, Geosystems* **18**, 2727-2747 (2017).
133. V. A. Kononova, Y. Y. Golubeva, O. A. Bogatikov, A. V. Kargin, Diamond resource potential of kimberlites from the Zimny Bereg field, Arkhangel'sk oblast. *Geology of Ore Deposits* **49**, 421-441 (2007).
134. M. G. Kopylova, P. Hayman, Petrology and textural classification of the Jericho kimberlite, northern Slave Province, Nunavut, Canada. *Canadian Journal of Earth Sciences* **45**, 701-723 (2008).
135. S. I. Kostrovitsky, T. Morikiyo, I. V. Serov, D. A. Yakovlev, A. A. Amirzhanov, Isotope-geochemical systematics of kimberlites and related rocks from the Siberian Platform. *Russian Geology and Geophysics* **48**, 272-290 (2007).
136. J. D. Kramers, J. C. M. Roddick, J. B. Dawson, Trace element and isotope studies on veined, metasomatic and "MARID" xenoliths from Bultfontein, South Africa. *Earth and Planetary Science Letters* **65**, 90-106 (1983).
137. Y. O. Larionova *et al.*, Kimberlite age in the Arkhangelsk Province, Russia: Isotopic geochronologic Rb–Sr and 40Ar/39Ar and mineralogical data on phlogopite. *Petrology* **24**, 562-593 (2016).
138. Q.-L. Li *et al.*, Precisely dating Paleozoic kimberlites in the North China Craton and Hf isotopic constraints on the evolution of the subcontinental lithospheric mantle. *Lithos* **126**, 127-134 (2011).
139. E. Lim, A. Giuliani, D. Phillips, K. Goemann, Origin of complex zoning in olivine from diverse, diamondiferous kimberlites and tectonic settings: Ekati (Canada), Alto Paranaiba (Brazil) and Kaalvallei (South Africa). *Mineralogy and Petrology* **112**, 539-554 (2018).
140. R. Maas, M. B. Kamenetsky, A. V. Sobolev, V. S. Kamenetsky, N. V. Sobolev, Sr, Nd, and Pb isotope evidence for a mantle origin of alkali chlorides and carbonates in the Udachnaya kimberlite, Siberia. *Geology* **33**, 549-552 (2005).
141. I. L. Mahotkin, S. A. Gibson, R. N. Thompson, D. Z. Zhuravlev, P. U. Zherdev, Late Devonian Diamondiferous Kimberlite and Alkaline Picrite (Proto-kimberlite?) Magmatism in the Arkhangelsk Region, NW Russia. *Journal of Petrology* **41**, 201-227 (2000).

142. A. H. Maria, F. B. Denny, J. A. DiPietro, K. F. Howard, M. D. King, Geochemistry and Sr-Nd isotopic compositions of Permian ultramafic lamprophyres in the Reelfoot Rift – Rough Creek Graben, southern Illinois and northwestern Kentucky. *Lithos* **340-341**, 191-208 (2019).
143. D. Phillips *et al.*, in *Proceedings of the 7th International Kimberlite Conference,* J. J. Gurney, J. L. Gurney, M. D. Pascoe, S. H. Richardson, Eds. (Red Roof Design, Cape Town, 1999), vol. 2, pp. 677-688.
144. N. Priyatkina, A. K. Khudoley, V. N. Ustinov, K. Kullerud, 1.92 Ga kimberlitic rocks from Kimozero, NW Russia: Their geochemistry, tectonic setting and unusual field occurrence. *Precambrian Research* **249**, 162-179 (2014).
145. J. Ritsema, A. Deuss, H. J. van Heijst, J. H. Woodhouse, S40RTS: a degree-40 shear-velocity model for the mantle from new Rayleigh wave dispersion, teleseismic traveltime and normal-mode splitting function measurements. *Geophysical Journal International* **184**, 1223-1236 (2011).
146. J. V. A. Robey *et al.*, in *Kimberlites and related rocks. 4th International Kimberlite Conference,* J. Ross *et al.*, Eds. (Geological Society of Australia, Perth, 1989), vol. 1, pp. 382-391.
147. D. N. Robinson, Magnetite-serpentine-calcite dykes at Premier Mine and aspects of their relationship to kimberlite and to carbonatite of alkalic carbonatite complexes. *Physics and Chemistry of the Earth* **9**, 61-70 (1975).
148. C. Sarkar, L. M. Heaman, D. G. Pearson, Duration and periodicity of kimberlite volcanic activity in the Lac de Gras kimberlite field, Canada and some recommendations for kimberlite geochronology. *Lithos* **218–219**, 155-166 (2015).
149. C. Sarkar *et al.*, Geochronology, classification and mantle source characteristics of kimberlites and related rocks from the Rae Craton, Melville Peninsula, Nunavut, Canada. *Mineralogy and Petrology* **112**, 653-672 (2018).
150. T. A. Scambos, Isotopic and trace-element characteristics of the Central Montana Alkalic Province kimberlite-alnoite suite. *Montana Bureau of Mines Special Publication* **100**, 93-109 (1991).
151. U. Scharer, F. Corfu, D. Demaiffe, U-Pb and Lu-Hf isotopes in baddeleyite and zircon megacrysts from the Mbuji-Mayi kimberlite: constraints on the subcontinental mantle. *Chemical Geology* **143**, 1-16 (1997).
152. S. R. Shee *et al.*, in *Kimberlites and Related Rocks. 4th International Kimberlite Conference,* J. Ross *et al.*, Eds. (Geological Society of Australia, Perth, 1989), vol. 1, pp. 60-82.
153. A. P. Smelov, A. I. Zaitsev, in *Proceedings of 10th International Kimberlite Conference: Volume One,* D. G. Pearson *et al.*, Eds. (Springer India, New Delhi, 2013), pp. 225-234.
154. C. B. Smith, Pb, Sr and Nd isotopic evidence for sources of southern African Cretaceous kimberlites. *Nature* **304**, 51-54 (1983).
155. C. B. Smith, H. L. Allsopp, J. D. Kramers, G. Hutchinson, J. C. Roddick, Emplacement ages of Jurassic-Cretaceous South African kimberlites by the Rb-Sr method on phlogopite and whole-rock samples. *Transaction of the Geological Society of South Africa* **88**, 249-266 (1985).
156. C. B. Smith, T. C. Clark, E. S. Barton, J. W. Bristow, Emplacement ages of kimberlite occurrences in the Prieska region, southwest border of the Kaapvaal Craton, South Africa. *Chemical Geology* **113**, 149-169 (1994).
157. N. Stamm *et al.*, Primary petrology, mineralogy and age of the Letšeng-la-Terae kimberlite (Lesotho, Southern Africa) and parental magmas of Group-I kimberlites. *Contributions to Mineralogy and Petrology* **173**, 76 (2018).

158. J. Sun *et al.*, Repeated kimberlite magmatism beneath Yakutia and its relationship to Siberian flood volcanism: Insights from in situ U–Pb and Sr–Nd perovskite isotope analysis. *Earth and Planetary Science Letters* **404**, 283-295 (2014).
159. S. Tappe *et al.*, Plates or plumes in the origin of kimberlites: U/Pb perovskite and Sr-Nd-Hf-Os-C-O isotope constraints from the Superior craton (Canada). *Chemical Geology* **455**, 57-83 (2017).
160. S. Tappe, B. A. Kjarsgaard, S. Kurszlaukis, G. M. Nowell, D. Phillips, Petrology and Nd–Hf Isotope Geochemistry of the Neoproterozoic Amon Kimberlite Sills, Baffin Island (Canada): Evidence for Deep Mantle Magmatic Activity Linked to Supercontinent Cycles. *Journal of Petrology* **55**, 2003-2042 (2014).
161. S. Tappe *et al.*, A fresh isotopic look at Greenland kimberlites: Cratonic mantle lithosphere imprint on deep source signal. *Earth and Planetary Science Letters* **305**, 235-248 (2011).
162. S. Tappe *et al.*, Sources and mobility of carbonate melts beneath cratons, with implications for deep carbon cycling, metasomatism and rift initiation. *Earth and Planetary Science Letters* **466**, 152-167 (2017).
163. S. Tappe, A. Steenfelt, T. Nielsen, Asthenospheric source of Neoproterozoic and Mesozoic kimberlites from the North Atlantic craton, West Greenland: New high-precision U-Pb and Sr-Nd isotope data on perovskite. *Chemical Geology* **320-321**, 113-127 (2012).
164. S. Tappe, A. Stracke, D. van Acken, H. Strauss, A. Luguet, Origins of kimberlites and carbonatites during continental collision – Insights beyond decoupled Nd-Hf isotopes. *Earth-Science Reviews* **208**, 103287 (2020).
165. R. Tappert *et al.*, The petrology of kimberlites from South Australia: Linking olivine macrocrystic and micaceous kimberlites. *Journal of Volcanology and Geothermal Research* **373**, 68-96 (2019).
166. L. A. Tompkins *et al.*, in *Proceedings of the 7th International Kimberlite Conference,* J. J. Gurney, J. L. Gurney, M. D. Pascoe, S. H. Richardson, Eds. (Red Roof Design, Cape Town, 1999), vol. 2, pp. 874-887.
167. M. Tovey, A. Giuliani, D. Phillips, S. Moss, Controls on the explosive emplacement of diamondiferous kimberlites: New insights from hypabyssal and pyroclastic units in the Diavik mine, Canada. *Lithos* **360-361**, 105410 (2020).
168. D. Weis, D. Demaiffe, A depleted mantle source for kimberlites from Zaire: Nd, Sr and Pb isotopic evidence. *Earth and Planetary Science Letters* **73**, 269-277 (1985).
169. F.-Y. Wu *et al.*, In situ U-Pb age determination and Nd isotopic analysis of perovskites from kimberlites in southern Africa and Somerset Island, Canada. *Lithos* **115**, 205-222 (2010).
170. Y.-H. Yang *et al.*, In situ perovskite Sr–Nd isotopic constraints on the petrogenesis of the Ordovician Mengyin kimberlites in the North China Craton. *Chemical Geology* **264**, 24-42 (2009).
171. G. M. Yaxley *et al.*, The discovery of kimberlites in Antarctica extends the vast Gondwanan Cretaceous province. *Nat Commun* **4**, 2921 (2013).
172. D. Zhang *et al.*, Perovskite and baddeleyite from kimberlitic intrusions in the Tarim large igneous province signal the onset of an end-Carboniferous mantle plume. *Earth and Planetary Science Letters* **361**, 238-248 (2013).
173. H. F. Zhang, Y. H. Yang, Emplacement age and Sr-Nd-Hf isotopic charcateristics of the diamoniferous kimberlites from the eastern North China Craton. *Acta Petrologica Sinica* **23**, 285-294 (2007).
174. S. E. Zurevinski, L. M. Heaman, R. A. Creaser, The origin of Triassic/Jurassic kimberlite magmatism, Canada: Two mantle sources revealed from the Sr-Nd isotopic

composition of groundmass perovskite. *Geochemistry, Geophysics, Geosystems* **12**, (2011).
175. K. Hosseini *et al.*, SubMachine: Web-Based Tools for Exploring Seismic Tomography and Other Models of Earth's Deep Interior. *Geochemistry, Geophysics, Geosystems* **19**, 1464-1483 (2018).